Small

Attenuated Glial Reactivity on Topographically Functionalized Poly(3,4-Ethylenedioxythiophene):P-Toluene Sulfonate (PEDOT:PTS) Neuroelectrodes Fabricated by Microimprint Lithography

--Manuscript Draft--

Manuscript Number:	smll.201800863R1
Full Title:	Attenuated Glial Reactivity on Topographically Functionalized Poly(3,4-Ethylenedioxythiophene):P-Toluene Sulfonate (PEDOT:PTS) Neuroelectrodes Fabricated by Microimprint Lithography
Article Type:	Full Paper
Section/Category:	
Keywords:	neural interfaces; functionalization; topographies; astrogliosis; inflammation
Corresponding Author:	Catalina Vallejo-Giraldo, Ph.D National University of Ireland Galway Galway, IRELAND
Additional Information:	
Question	**Response**
Please submit a plain text version of your cover letter here. **If you are submitting a revision of your manuscript, please do not overwrite your original cover letter. There is an opportunity for you to provide your responses to the reviewers later; please do not add them here**.	17th April 2018 Dear Dr Ulf Scheffler: On behalf of all authors, I would like to express our gratitude to the reviewer for the comments. We have carefully gone through each comment made and have provided a response below. We have also made appropriate modifications to the manuscript, highlighted in blue font. We hope that the manuscript is acceptable in its present form and look forward to hearing your decision, and the decision of the referee. Thank you in advance for considering our revised submission. On behalf of the authors Yours sincerely, Catalina Vallejo Giraldo, PhD Centre for Research in Medical Devices (CÚRAM) National University of Ireland, Galway
Do you or any of your co-authors have a conflict of interest to declare?	No. The authors declare no conflict of interest.
Corresponding Author Secondary Information:	
Corresponding Author's Institution:	National University of Ireland Galway
Corresponding Author's Secondary Institution:	
First Author:	Catalina Vallejo-Giraldo, Ph.D
First Author Secondary Information:	
Order of Authors:	Catalina Vallejo-Giraldo, Ph.D
	Katarzyna Krukiewicz, PhD
	Ivo Calaresu

	Jingyuan Zhu
	Matteo Palma
	Marc Fernandez
	Benjamin G
	Nathalia Peixoto
	Nazar Nazar Farid
	Gerard O'Connor
	Laura Ballerini
	Abhay Pandit
	Manus Jonathan Paul Biggs
Order of Authors Secondary Information:	
Abstract:	Following implantation, neuroelectrode functionality is susceptible to deterioration via reactive host cell response and glial scar-induced encapsulation.Within the neuroengineering community there is a consensus that the induction of selective adhesion and regulated cellular interaction at the tissue-electrode interface can significantly enhance device interfacing and functionality in vivo.In particular, topographical modification holds promise for the development of functionalized neural interfaces to mediate initial cell adhesion and the subsequent evolution of gliosis, minimizing the onset of a pro-inflammatory glial phenotype, to provide long-term stability. Herein, a novel low-temperature microimprint-lithography technique for the development of micro-topographically functionalized neuroelectrode interfaces in electrodeposited PEDOT:PTS is described and assessed in vitro. Platinum (Pt) microelectrodes were subjected to electrodeposition of a PEDOT:PTS microcoating which was subsequently topographically functionalized with an ordered array of micro-pits,inducing a significant reduction in electrode electrical impedance and an increase in charge storage capacity.Furthermore, topographical functionalized electrodes reduced the adhesion of reactive astrocytes in vitro, evident from morphological changes in cell area, focal adhesion formation, and the synthesis of pro-inflammatory cytokines and chemokine factors.This study contributes to the understanding of gliosis in complex primary mixed cell cultures,and describes the role of micro-topographically modified neural interfaces in the development of stable microelectrode interfaces.

WILEY-VCH

DOI: 10.1002/ ((please add manuscript number))
Article type: Full Paper

Attenuated Glial Reactivity on Topographically Functionalized Poly(3,4-Ethylenedioxythiophene):P-Toluene Sulfonate (PEDOT:PTS) Neuroelectrodes Fabricated by Microimprint Lithography

Catalina Vallejo-Giraldo, Katarzyna Krukiewicz, Ivo Calaresu, Jingyuan Zhu, Matteo Palma, Marc Fernandez, Benjamin G, Nathalia Peixoto, Nazar Farid, Gerard O'Connor, Laura Ballerini, Abhay Pandit, and Manus Jonathan Paul Biggs*

Dr Catalina Vallejo-Giraldo, [+]Dr Katarzyna Krukiewicz, MSc Marc Fernandez, Prof. Abhay Pandit, Dr Manus Jonathan Paul Biggs
CÚRAM - Centre for Research in Medical Devices – Galway, Biosciences Research Building, 118 Corrib Village, Newcastle, Galway, Ireland
E-mail: catalina.vallejogiraldo@nuigalway.ie
[+] Department of Physical Chemistry and Technology of Polymers
Silesian University of Technology, Gliwice, Poland
Dr Matteo Palma, MSc Jingyuan Zhu
School of Biological and Chemical Sciences, Queen Mary University of London, Mile End Road, London E14NS, UK
Dr Nathalia Peixoto, MSc Benjamin G
Department of Electrical and Computer Engineering, George Mason University, 4400 University Drive MS-1G5
Dr Nazar Farid, Dr Gerard O'Connor
School of Physics, National University of Ireland, Galway, University Road, Galway, Ireland
MSc Ivo Calaresu, Prof. Laura Ballerini
Scuola Internazionale Superiore di Studi Avanzati (SISSA), Via Bonomea, 265, 34136,Trieste, Italy

Keywords: neural interfaces, functionalization, topographies, astrogliosis, inflammation

Following implantation, neuroelectrode functionality is susceptible to deterioration via reactive host cell response and glial scar-induced encapsulation. Within the neuroengineering community there is a consensus that the induction of selective adhesion and regulated cellular interaction at the tissue-electrode interface can significantly enhance device interfacing and functionality *in vivo*. In particular, topographical modification holds promise for the development of functionalized neural interfaces to mediate initial cell adhesion and the subsequent evolution of gliosis, minimizing the onset of a pro-inflammatory glial phenotype, to provide long-term stability. Herein, a novel low-temperature microimprint-lithography

technique for the development of micro-topographically functionalized neuroelectrode interfaces in electrodeposited PEDOT:PTS is described and assessed *in vitro*.

Platinum (Pt) microelectrodes were subjected to electrodeposition of a PEDOT:PTS microcoating which was subsequently topographically functionalized with an ordered array of micro-pits, inducing a significant reduction in electrode electrical impedance and an increase in charge storage capacity. Furthermore, topographical functionalized electrodes reduced the adhesion of reactive astrocytes *in vitro*, evident from morphological changes in cell area, focal adhesion formation, and the synthesis of pro-inflammatory cytokines and chemokine factors. This study contributes to the understanding of gliosis in complex primary mixed cell cultures, and describes the role of micro-topographically modified neural interfaces in the development of stable microelectrode interfaces.

1. Introduction

Implantable stimulation and recording devices have received significant attention in biomedical engineering and have brought great success in the treatment of central nervous system disorders including paralysis, [1] epilepsy [2] and Parkinson's disease. [3, 4] In order to achieve chronic functionality and integration with surrounding tissue, material functionalization strategies have been employed to provide chemical and physicomechanical properties analogous to neural tissues, with an ultimate goal of mitigating electrode deterioration via reactive host cell response and glial scar-induced encapsulation.[3, 5-8]

From this perspective the field of neuroelectrode engineering has encouraged the use of alternative electroactive materials over conventional metallic strategies such as gold and platinum [9, 10] as an approach to provide an electrochemical platform for the immobilization of biological molecules [11, 12] or in order to promote physicomechanical mimicry through soft or topographically rough interfaces. [13, 14] Specifically, semiconducting polymers,[6, 15-20] including polypyrrole (PPy) [21-23] and poly(3,4-ethylenedioxythiophene) (PEDOT), [24-26] and

their hybrids [27, 28] have been employed widely in neural engineering because of their versatility as electrode coatings through electrodeposition processes, [29, 30] and have been employed to enhance the neuroelectrode electrochemical profile, [26, 31] and provide a platform for chemical, [32-34] and morphological [35-38] functionalization to meet particular requirements. [39-42]

Ongoing studies into topographical functionalization strategies of the neural interface have explored the micro [43-45] to the nanoscale [46, 47] and have shown promise, in promoting a low impedance profile of implantable electrodes through effects on electrode surface area. [46, 48, 49] Recent studies indicate the cytocompatibility of conducting and semiconducting polymers *in vitro* and *in vivo* and the realization that electrodeposited conducting coatings present a nano-rough surface has led to speculation that topography may play a role in directing the cellular functional response to implanted electrodes by modulating cell function through altering integrin distribution,[50] and differential cell adhesion. [51, 52] In particular nanotopographically functionalized materials have been shown to influence the activation of intrinsic cellular processes that lead to more quiescent or reactive cell phenotypes in the onset of a pro-inflammatory response [46, 50-53] and glial scar formation. [54, 55]

Ordered arrays of lithography fabricated nanopit substrates have been consistently shown in previous work to disrupt cell adhesion *in vitro* by direct or indirect modulation of focal adhesion formation. [51, 52] Recent *in vitro* studies exploring topographical modification have been successful in controlling astrocyte adhesion while promoting high neuron integration as strategies to reduce gliosis, [14, 56, 57] with microscale isotropic pit topographies of 1 μm in depth reported to modulate astrocytes adhesion *in vitro.* [61]

Although neural cells are reported to produce sparse and small focal adhesions, [58] it has been shown that astrocytes are adhesion dependent,[59] and will form a monolayer in culture, providing neurons with physicochemical cues, to modulate neural processes extension.[57] Consequently, the ability to control astrocyte adhesion and promote a reduction of the reactive

astrocyte phenotype at the electrode interface is critical to support neuronal outgrowth,[60] and reduce glial scar formation.[54]

In this study, PEDOT:PTS coated microelectrodes were topographically functionalized with ordered micro-pit arrays using a novel low-temperature three-step die imprinting lithography process, as a strategy to enhance electrode functionality, cytocompatibility and promote selective adhesion, minimizing the onset of a pro-inflammatory glial phenotype, in neural applications. The physical, electrochemical and cytocompatibility effects of topographically functionalized microelectrodes were subsequently explored *in vitro*. Our results elucidate important topographical effects with regard to microelectrode functionality, cytocompatibility and astrogliosis towards the generation of neural interfaces with superior electrical and biological properties.

2. Results and Discussion

2.1. Physical Characterization

A range of techniques have been explored to create defined microstructures on electrode surfaces, [62] including laser ablation, [63, 64] focused ion beam, [65, 66] sputter etching, [67, 68] reactive ion etching, [69, 70] deep reactive ion etching, [71, 72] hot embossing, [73, 74] and electron beam lithography.[75,76] Complementary to these techniques, imprint lithography is an especially attractive approach due to its simplicity, non-destructive character and feasibility of patterning large areas with features down to 10 nm using elevated temperature and/or pressure processes to transfer a pattern into typically thermoplastic materials.[77-80] Regarding the variation of imprinting methods, direct die imprinting is of particular interest as patterns are transferred via a stamp/die in a single imprint process. [81] However, the quality of the pattern transfer depends on relatively high temperatures and pressures [81, 82] and silanization steps are also required to facilitate the separation of the die and imprinted material. [83-86]

A study by Tan et al. [87] shows the imprinting process of non-thermoplastic materials such as PEDOT and chitosan using plasticizers. Imprinting of PEDOT and chitosan films from the

poly(dimethylsiloxane) mold was achieved at a pressure of 10 kPa and 25 °C by controlled addition of glycerol as a plasticizer. In this case, the added glycerol was used to increase the chain mobility of the polymers, resulting in lower imprinting temperature and low pressures. Further, a room temperature nanoimprint lithography process was shown by Pisignano and colleagues [88] with the nanoimprinting of patterns in organic semiconductors with poor thermoplastic properties.

A focus of this study was to develop a low-temperature, simple imprinting method to reproduce lithographically fabricated well-defined and ordered topographies into PEDOT:PTS electrodeposited electrode coatings. Critically this approach preserves the ability to introduce coupled biochemical functionalization – an approach which has been explored extensively with PEDOT functionalized microelectrodes. [89-92] Arrays of pits possessing a diameter of ~1 µm a pitch of ~2 µm and depth of ~ 1 µm were initially fabricated via photolithography which was used as a mask for a Ni (Nickel) electroforming process as described previously.[51] Fabricated negative Ni masters were used as hard stamps to replicate the original topography into electrodeposited PEDOT:PTS coatings via an imprint process applying 1.9 metric tons per cm^2 for fifteen minutes to achieve high quality pattern transfer conducted at room temperature. To facilitate substrate separation, a dehydration-assisted process was employed to enhance the cohesion of PEDOT:PTS and prevent topography disruption during the separation step, ensuring high pattern transfer as first described by Yang et al. [83] who also used the dehydration-assisted method for the imprinting of spin-coated PEDOT:PSS nanogratings for photovoltaic applications. In this way, silanization steps were avoided as they caused neural cell death to our cultures due to insufficient evaporation of fluorides. [93, 94]

Experimentally, the micro-imprinting process is outlined in **Figure 1.** Representative SEM micrographs of the nickel die used in the imprinting process and the resulting well-ordered arrays of micro-pits in the micro-topographically functionalized PEDOT:PTS coated

microelectrodes with respective dimensions are indicated in **Figure S1A**. The calculated thickness of the electrodeposited PEDOT:PTS coating was of 1.22 ± 0.12 µm.

Following imprinting, PEDOT:PTS microelectrodes were micro-topographically functionalized with arrays of pits with a diameter of 0.82 ± 0.07 µm and interpit spacing of 2.28 ± 0.06 µm. The depth was confirmed by AFM analysis **(Figure 1SB)** indicating vertical distances of 0.96 ± 0.07 µm and high fidelity pattern transfer using a low temperature three-step die imprinting lithography process. No Ni residues from the die master on the micro-topographically functionalized PEDOT:PTS coated microelectrodes were present after the imprinting process **(Table S1).**

The topographical profiles of micro-imprinted PEDOT:PTS coated microelectrodes were subsequently analyzed by AFM and results presented relative to pristine PEDOT:PTS and to a PEDOT:PTS coated microelectrode flattened via imprinting with a planar glass substrate, these control groups serving as pristine electrodeposited PEDOT:PTS surface and a topographically planar PEDOT:PTS surface respectively. A sputtered platinum (Pt) group was also used as a representative electrode control material (images shown in **Figure S2**). Representative SEM and AFM images of experimental groups are depicted in **Figure 2** (A-B). Micro-topographically functionalized PEDOT:PTS coated microelectrodes resulted in a non-significant decrease in surface roughness (R_a) relative to pristine PEDOT:PTS coated microelectrode but in a significant increase when compared to the control flattened PEDOT:PTS coated microelectrodes **(Table 1).** Pristine PEDOT:PTS coated microelectrodes exhibited an average roughness of 85 nm over 10 μm^2, and an average roughness of 53 nm and 76 nm was noted on flattened and micro-topographically functionalized electrodes respectively. All PEDOT:PTS coated electrodes exhibited a significant increase in surface roughness (R_a) relative to Pt microelectrodes, which possessed an experimental R_a of 2 nm over 10 μm^2.[49]

The micro-imprinting process resulted in a reduction in R_a of the inter-pit surface to levels similar to flattened PEDOT:PTS electrodes, indicating that the application of the mechanical imprinting eliminated nano-roughness while producing a regular micropit topography.[95] Significantly, the calculated physical surface area of the micro-topographically functionalized PEDOT:PTS coated microelectrodes was of 2.35 E+10 nm^2 ± 51.77 E+06 nm^2, 1.74 E+10 nm^2 ± 93.34 E+06 nm^2 for the pristine PEDOT:PTS coated microelectrodes 1.32 E+10 nm^2 ± 71.42 E+06 nm^2 for the flattened PEDOT:PTS coated microelectrodes and 1.05 E+10 nm^2 ± 35.35 E+06 nm^2 for sputtered Pt electrodes indicating that through micro-imprinting the surface area of electrodeposited PEDOT:PTS was significantly increased relative to nano-rough pristine electrodeposited materials and uncoated Pt electrodes as shown in Table 1. These results suggest that micro-imprinting functionalization of PEDOT:PTS coated microelectrodes can be employed to induce a 135.06 % greater surface area relative to pristine PEDOT:PEDOT coated microelectrodes and a 178.03 % greater surface area relative to flattened control microelectrodes. Critically, micro-topographically modified PEDOT:PTS coated microelectrodes represented a 223.81 % increase in surface area over that of Pt microelectrodes.

2.2. Electrochemical Characterization

Topographical surface modification of the neural electrodes has shown promise in improving the electrochemical performance through high aspect ratio structures, increasing the active surface area of the electrodes. [13, 62] The electrochemical performance and the evaluation of the resulting effective-active surface area of the functionalized microelectrodes were subsequently assessed. To allow comparison, the evaluation of the electrochemical profile of in-house fabricated sputtered Pt microelectrodes was compared to topographically and non-topographically modified electrodeposited PEDOT:PTS electrodes and to electrodeposited gold coated microelectrodes with a similar experimental coating thickness of the as-formed PEDOT:PTS coatings, which possessed an approximated thickness of 1.21 ± 0.08 µm and 1.22 ± 0.12 µm, respectively.

Figure 3A shows the CVs for each of the experimental and control groups in 1X phosphate-buffered saline (PBS) evaluated with a microelectrode area of 0.287 mm^2. The increase in CSC **(Table 2)**, which was approximated through the integration of the charge passed within one CV scan, confirmed the presence of highly conducting PEDOT:PTS coatings with improvement in the electrochemical performance of the microelectrodes over that of bare platinum and gold coated microelectrode controls.[96, 97] In addition, and owing to the topographical functionalization, further enhancement of electrical performance was observed over that of the CSC of the PEDOT:PTS coated microelectrodes. The highest CSC was obtained with the micro-topographically functionalized PEDOT:PTS coated microelectrodes with a capacitance of 131.01 ± 8.05 μC mm^{-2} followed by the pristine PEDOT:PTS coated microelectrodes with a CSC of 48.82 ± 0.49 μC mm^{-2} and finally the controlled non-patterned surface, flattened PEDOT:PTS coated microelectrodes, with a CSC of 19.09 ± 0.77 μC mm^{-2} (Table 2). Of note is that these wide ranges of the aforementioned CSC values suggest that film structure plays a major role in determining the capacitance; more specifically, this may be related to the role of volumetric capacitance, significantly reduced on the flattened PEDOT:PTS coated microelectrodes.[98] The flattening geometry may be limiting the volume fraction of the coating, hence limiting the favorable packing of the polymeric coating for facile ion transport affecting the capacitance.[98]

Furthermore, and together with the increased charge storage capacity, micro-topographically functionalized PEDOT:PTS coated microelectrodes possessed a significantly increased effective electroactive surface area relative to pristine and flattened PEDOT:PTS coated microelectrodes, and increased even further when compared with the bare platinum and gold coated microelectrodes. The electroactive surface area was measured using a redox probe (2.5 mol dm^{-3} $K_4[Fe(CN)_6]$ in 0.1 M KCl) solution and estimated according to the Randles-Sevcik equation (**Equation 1**). Figure 3B shows that it is enough to deposit an electroactive PEDOT:PTS layer on the surface of Pt microelectrodes to observe a 5X increase in effective

surface area, also reported in previous studies into electroactive polymers.[99-100] Further, micro-pit functionalization resulted in a 2X increase in the microelectrode electroactive surface area relative to pristine PEDOT:PTS coated microelectrodes. Likewise, the micro-topographically functionalized PEDOT:PTS coated microelectrodes induced a significant 12X increase in effective surface area relative to Pt microelectrodes and a significant 11X increase relative to gold coated microelectrodes. It is noteworthy, that electroactive surface area between bare platinum and gold coated microelectrode controls were not significantly different.

Following PEDOT:PTS coated microelectrode flattening via imprinting with a planar glass substrate, microelectrode effective surface area was decreased relative to both micro-topographically functionalized and pristine PEDOT:PTS coated microelectrodes. This is due to an overall reduction of microelectrode surface area and lower R_a when compared to the pristine and PEDOT:PTS functionalized microelectrodes. However, flattened PEDOT:PTS microelectrodes still possessed an increased electroactive surface area relative to bare platinum and gold coated microelectrodes.[49] The evolution of electroactive surface area is of importance for microelectrodes, especially because the currents measured with implanted neural recording devices are in the range of µA or below. [101-104] This, together with the non-typical shape of CVs, [105] makes the process of optimization of microelectrode modification a challenging task. Complimentary data obtained with larger electrodes (1.6 cm^2) as part of the optimization process for this work is presented in **Figure S3**.

Comparative electrochemical impedance spectroscopy (EIS) profiles of all experimentally modified microelectrodes are presented in the form of a Bode diagram **(**Figure 3C**)** and Nyquist plot (Figure 3D). Overall, micro-topographically functionalized PEDOT:PTS microelectrodes exhibited the lowest impedance profile within the 0.1 Hz to 100 kHz frequency range, lower than that of pristine PEDOT:PTS microelectrodes and significantly lower than that of gold coated and bare platinum microelectrodes. This indicates the superior electrical performance of electrodes subjected to micro-topographical functionalization and the diminishing effect of the

process of PEDOT:PTS flattening on the electrochemical properties of microelectrodes, due to the impact of the former on volumetric changes of the coating. [98]

The detailed insight into the process of charge transport was possible by the simulation of EIS data with an equivalent electrical circuit. As shown in Figure 3D, a Randles equivalent circuit [106, 107] was indicated as the most appropriate and was used to fit the impedance data. The parameters of the equivalent circuit included the solution resistance (R_s), resistance of microelectrodes (R_m), constant phase element (CPE_1) and the diffusion impedance (Z_w) (replaced with CPE_2 in the case of flattened PEDOT:PTS coated microelectrodes and gold coated microelectrodes). The simulated data confirmed the lowest resistance of micro-topographically functionalized PEDOT:PTS coated microelectrode (3.11 ± 0.13 kΩ), when compared to pristine (12.01 ± 1.53 kΩ) and flattened (357.77 ± 14.64 kΩ) PEDOT:PTS coated microelectrodes, as well as bare platinum (40.28 ± 0.63 kΩ) and gold coated (23.61 ± 1.28 kΩ) microelectrodes. The summary of resistance calculated values is tabulated in **Table 3**.

The range of impedance as well as the magnitude of resistance achieved by micro-topographically functionalized PEDOT:PTS microelectrodes place them among the surface-materials suitable for use in neural stimulation and recording. [108, 109]

To further confirm the effects of micro-pit topographical functionalization on enhancing the electrical performance of the PEDOT:PTS coated microelectrode through an increase in surface area, force-controlled current-voltage (I-V) spectra where recorded employing conductive-AFM (C-AFM) (in PeakForce Tuna mode, PF Tuna, Bruker) using a system detailed in **Figure S4**. Figure 3E shows the surface topography and the corresponding distribution of the electrical profile at the nanoscale level within a micro-topographically functionalized PEDOT:PTS coated microelectrode, respectively. The comparative I-V curves provide additional insights into the role of the micro-pit topography in generating lower resistance profiles of the PEDOT:PTS relative to non-imprinted peri-pit regions. This effect is likely due to a differential

response in potential across the pit, resulting in a linear increase in current compared to a steady response seen on the I-V relationship from the non-patterned region.

In order to determine the stability of PEDOT:PTS functionalized microelectrodes, substrates were subjected to 500 cycles of continuous potentiodynamic stimulation with the aim of testing, under working conditions, the durability and the electrochemical robustness of the potential neural electrodes. [8, 110, 111] The loss in electroactivity of the microelectrodes was calculated as a percentage based on CSCs recorded before and after stability studies (Table 2). A high loss in CSC was observed for Pt sputtered microelectrodes due to the thickness differences, with a 72 % loss. In contrast, with a comparable working thickness obtained with gold coated microelectrodes, a significantly lower percentage loss of 37 % was observed which was similar to the percentage loss obtained with PEDOT:PTS coated microelectrodes. Significantly, flattened PEDOT:PTS coated microelectrodes were associated with an diminution of performance, with a loss of 98 %. Overall, superior electrochemical stability and robustness was observed with micro-topographically functionalized PEDOT:PTS coated microelectrodes with an electroactivity loss of 26 %. This stability effect, coupled with the high effective surface area and the low impedance profiles, identifies the micro-topographically functionalized PEDOT:PTS coated microelectrodes developed here, as functionalized microelectrodes with potential in neural stimulation and recording performance.

2.3. Biological Characterization

Neural interfaces that promote neural integration, with a minimal inflammation response are persistent challenges within the realms of biomaterials and neural engineering. Even though the cellular response to topography is cell specific, it has been shown that topographical modifications may contribute significantly to addressing the challenges of selective cell adhesion and modulated cell behavior to reduce gliosis at the material-tissue interface.[112]

The neural response to micro-pit topographies replicated in PEDOT:PTS coated 1.6 cm^2 Pt electrodes was evaluated using primary VM mixed neural cell population *in vitro* **Figure S5**.

Topographical functionalization to modulate differential cell adhesion and the observation that flat or non-structured electrodes surfaces favor astrocyte adhesion has been reported previously.[14, 56, 113] A recent study by Seker and colleagues[56] demonstrated the efficacy of nanotopographical modification of the electrode surface in reducing focal adhesion formation in astrocytes while maintaining neural integration on np-Au surfaces. Conversely, Qi et al.[114] showed that micro-patterned topographies, with dimensions ranging from 2 µm - 10 µm, influence the differentiation of adult neural stem cells (ANSCs) into neurons, and may discourage the differentiation of astrocytes.

Figure 4A shows representative fluorescent micrographs of VM derived mixed cultures of neurons and astrocytes cultured on experimental and control electrodes. All groups were evaluated over a period of three, seven and ten days in culture. The persistence of neurons and astrocytes on each of the experimental and control groups as a function of time is presented in Figure 4B**.** The percentage cell density of astrocytes and neurons on each assessed group initially indicated that flattened PEDOT:PTS electrodes induced a significant linear increase of astrocytic presence as a function of time, with a subsequent significant decrease in neuronal presence relative to all experimental and the bare platinum control substrates. By day ten, the flattened PEDOT:PTS coated electrodes exhibited an astrocyte presence of 97.67 % and a 2.32 % neuron presence. Interestingly, pristine PEDOT:PTS coated electrodes induced a significant decrease in astrocytic presence and a significant increase in neuron cell populations present at each time point relative to all the experimental and control groups. Following ten days in culture, the astrocyte and neuron presence on pristine PEDOT:PTS coated electrodes was 46.39 % and 53.60% respectively. Furthermore, when comparing the neuron and astrocyte cell density populations with control platinum and micro-topographically functionalized PEDOT:PTS coated electrodes, an identical trend with no statistical difference was observed for differential neuron or astrocytes density over time. Following ten days in culture, the astrocyte population on control platinum and micro-topographically PEDOT:PTS coated

electrodes was recorded at 61.97 % and 62.46 % respectively, 16% greater than that on pristine PEDOT:PTS coated electrodes.

In conjunction with cell density, as an indicator of cell viability neurite length on experimental and control substrates was also analyzed **(**Figure 4C**).** At day three, a significant decrease in neural length was observed on all experimental groups relative to Pt electrodes on which mean neurite length was 175.08 µm ± 10.55. This trend was lost by day seven and a linear increase in length as a function of electrode surface area was observed. However, neurite length on mechanical flattened control samples could not be quantified due to a significant reduction in neuron presence, making the application of the stereology method used for the quantification of length invalid.

Further significant differences in neural length were observed by day ten, with significant neurite elongation exhibited in cells cultured on micro-topographically functionalized PEDOT:PTS electrodes (607.68 µm ± 5.53) relative to Pt control (566.36 µm ± 6.35) and pristine PEDOT:PTS coated electrodes (325.76 µm ± 4.66).

These results indicate that pristine PEDOT:PTS coatings do not enhance astrocyte proliferation and adhesion relative to control Pt electrodes and that micropatterning of PEDOT:PTS coatings can be employed to significantly enhance neurite length *in vitro*. Conversely, mechanically flattened PEDOT:PTS coated electrodes induced overall poor viability/adhesion of the primary mixed VM cell population relative to all other experimental conditions. [14, 113] That neurons cultured on pristine PEDOT:PTS coated electrodes exhibited a higher frequency but with significantly shorter neural processes relative to Pt electrodes and micro-topographically functionalized PEDOT:PTS coated electrodes may suggest that network development in ventral mesencephalic derived neurons is not entirely supported on nano-roughened, pristine electrodes.[115, 116] Critically, VM derived glial cells promote neuronal survival and neurite growth by releasing growth factors and providing an ideal biochemical milieu *in vitro* for neuronal development.[115] Thus, although pristine PEDOT:PTS coated electrodes were

associated with a significant reduction in astrocyte density and promoted more neural coverage relative to cell population ratios observed on bare platinum and micro-topographically functionalized PEDOT:PTS coated electrodes, this phenomenon did not translate into the development of an extensively interconnected functional neural network. Rather, it may suggest the onset of a pro-inflammatory response.[115] Neurite length was significantly increased on the micro-topographically functionalized PEDOT:PTS coated electrodes by day ten relative to all experimental groups, suggesting that neurons may benefit from the presence of an underlying glia network and a morphological response to micro-topographical features may be manifest in enhanced neurite extension. This observation is supported by previous research into topographical features supporting neural outgrowth through supportive cues. [84, 117-119] Also, it can be inferred that neurite extension on micro-topographically functionalized PEDOT:PTS coated electrodes may suggest a reduced inflammatory environment from the glial interactions relative to all experimental and control groups. [115]

In order to assess the reactivity of astrocytes (the key players in astrogliosis) on fabricated electrodes, the mean cellular area was quantified as a morphological indicator of a reactive astrocyte phenotype again using a primary VM mixed cell culture model. Critically, morphological analysis of astrocyte populations has been shown repeatedly to provide helpful insights into resting or activated functional states in astrogliosis, considering astrocytic heterogeneity. [120,121] Furthermore, to assess modulated astrocyte morphology and adhesion on experimental electrodes, GFAP immunofluorescent labeling was conducted in conjunction with Paxillin labeling, a key focal adhesion protein (**Figure 5A**). It has been shown *in vitro* that in 2D cultures neurons will grow on the dorsal surface and extend processes along topographical cues provided by an astrocyte monolayer.[57] Consequently, it has been suggested that astrocyte presence on an implanted electrode is critical to support neural integration and neurite outgrowth [60] rather, it is the reduction of a reactive astrocyte phenotype presence that is a

potential functionalization strategy in minimizing astrogliosis in peri-electrode glial scar formation.[54]

Representative fluorescent micrographs of isolated astrocytes from the mixed primary VM cell cultures grown on controls Pt, and experimental PEDOT:PTS functionalized electrodes were captured over three, seven and ten days in culture (Figure 5A). Figure 5B represents the distribution of astrocyte cell areas as a function of GFAP staining over time. The distribution of the astrocyte cell area is significantly shifted towards a greater astrocyte cell area on Pt electrodes relative to pristine PEDOT:PTS, flattened PEDOT:PTS and micro-topographically functionalized PEDOT:PTS coated electrodes. By day ten, the frequency of astrocyte cell areas between the ranges of 450 μm^2 and 2250 μm^2 on Pt electrodes was significantly increased. Astrocyte cultured on pristine PEDOT:PTS, flattened PEDOT:PTS and micro-topographically functionalized PEDOT:PTS coated electrodes, however, exhibited a bio-modal distribution of cell area, with significant peaks also observed in the 50-350 μm^2 cell area range. Interestingly, micro-topographically functionalized PEDOT:PTS coated electrodes were associated with the lowest astrocyte area distribution when compared to control and experimental substrates at all time points. It was observed by day ten that the 80 % of the astrocyte cell areas were confined within the ranges of 100 μm^2 and 1250 μm^2. These findings are particularly important as it has been shown that the variations in overall astrocytic cell area underlie reactivity implications over time,[120, 122, 123] where enlarged astrocytes areas may translate into moderate and/or severe reactive astrogliosis.[122]

Of further interest is the observation that the increased frequency of astrocytes with enlarged cell areas observed on bare platinum, pristine PEDOT:PTS and flattened coated electrodes is associated with a reduction in neural outgrowth relative to neurons cultured on micro-functionalized PEDOT:PTS electrodes, again pointing to a reactive astrocyte induced disruption of network evolution. This effect was largely accentuated on flattened PEDOT:PTS coated electrodes.

In order to evaluate perturbation of assessed electrode topography on astrocyte adhesion and to draw parallels between reactive astrocyte phenotype and focal adhesion formation, quantification of mean cellular focal adhesion number and length was carried out (Figure 5C-D). The regulation of focal adhesion formation in adherent cells such as astrocytes, involves complex recruitment of integrin-dependent signaling pathways mainly mediated by non-receptor tyrosine kinases, markedly by focal adhesion kinase (FAK).[124] Further, it has been shown that mediated signaling through FAK/Paxillian in astrocytes plays an important role in astrocyte cell morphology, where a reduction of tyrosine phosphorylation and paxillin expression is related to the stellation of astrocytes. [125-127] However, in pathological situations, astrocytes no longer adopt a stellar appearance but become hypertrophic in morphology, and are associated with increased focal adhesion signaling, so-called reactive astrocytes. [128-131] Certainly, cell-adhesion is mainly controlled through cell-substrate interactions, where topographies have been shown to play an essential role. [50]

Analysis of the distribution of FA frequency and length in astrocytes on bare platinum electrodes indicated that at day three 70% of the astrocytes exhibited ten focal adhesion contacts per astrocyte with lengths ranging between 0.5 µm and 10 µm. By day ten, a significant increase in astrocytes adhesion was observed with 70% of the astrocytes exhibiting between 15 and 70 focal adhesion points per cell with maintained focal adhesion lengths between the ranges of 0.5 µm and 8 µm compared to day three. These results suggest a decrease of cell motility owing to the higher number of focal adhesion contacts per cell, but further to the stable lengths achieved, [52] results that in light of the augmented astrocytic cell areas observed on these electrodes, showed the development of more focal adhesion contacts suggesting the presence of a more reactive astrocyte phenotype. In addition, bare platinum (R_a : 2 nm) commonly used in neural electrodes, does not allow for the selective control of cell adhesion (Figure 5B), which together with its mechanical rigidity, may account for the overall higher reactive astrocyte presence than that of more compliant conducting polymeric coated electrodes. [132]

On the other hand, the pristine PEDOT:PTS coated electrodes, the flattened PEDOT:PTS coated electrodes, and the micro-topographically functionalized PEDOT:PTS coated electrodes, were associated with similar astrocyte adhesion over time, with overall focal adhesion numbers significantly less than those observed on bare platinum electrodes.

By day ten, more than 80% of the astrocytes on both, pristine PEDOT:PTS and the flattened PEDOT:PTS coated electrodes, presented a mean value of fifteen focal adhesions per cell. Conversely, micro-topographically functionalized PEDOT:PTS coated electrodes, induced significant modulation to the distribution of the number of astrocyte focal adhesion with 38% of the astrocyte population exhibiting an increase in the mean number of focal adhesions per cell of between 15 and 50 focal adhesions per astrocyte. This observation together with the comparatively lower astrocyte areas observed on the micro-topographically functionalized PEDOT:PTS coated electrodes, may allude to a differential effect in astrocyte adhesion and a reduction in reactive astrocytes presence as a function of micro-topographical modification. The length of the astrocyte focal adhesion points did not change significantly over time on flattened PEDOT:PTS coated electrodes and on micro-topographically functionalized PEDOT:PTS coated electrodes, with lengths confined between the ranges of 0.5 µm and 5 µm. In contrast, pristine PEDOT:PTS coated electrodes resulted in shorter astrocyte focal adhesion contact lengths between the ranges of 1 µm and 1.5 µm by day ten.

It has been shown by our studies in other fields that ordered nanopits topographies are proposed to impair focal adhesion formation by disrupting integrin activation and clustering, an effect enhanced at the microscale length. [50, 51, 56, 59] Indeed, experimentally this work has shown that PEDOT:PTS coated electrodes functionalized with a micro-pit topography have a significant influence on reactive astrocyte adhesion. Furthermore, these findings present opportunities to study reactive astrocyte presence through cytoskeleton-linked proteins signaling mechanisms controlling astrocyte phenotype.

Understanding the glia interactions as key contributors in the glial scar formation is essential [54] and in addition to influencing cytoskeleton-linked proteins, substrate topography has been previously shown to affect cellular function and the synthesis of cytokines and signaling molecules in neural cells.[133, 134] To elucidate further the roles of topographical functionalization on the neural response *in vitro*, changes in the expression of pro-inflammatory cytokines and chemokine factors were assessed via multiplex ELISA analysis. Currently, few studies have examined the effect of topographical functionalization on the glial cell functional response in complex mixed cell cultures. [75] With this in mind, glial-derived cytokines and chemokine factors such as IFN-γ, TNF-α, IL-6, IL-5, and KC/GRO, involved in mediating neuronal-glial interactions and modulation of reactive astrogliosis were selected for analysis. [135-140] The release profiles were compared between each of the experimental groups, controls and with an additional inflammatory control group, VM cells cultured on Thermanox® Plastic Coverslips (tissue culture plastic) which received a stimulus of interleukin-1beta (IL-1β) at a dose of 10 ng ml^{-1}. Complementary data for the optimization of the different concentrations of IL-1β as inflammatory stimuli on VM cells cultures is shown in **Figure S6** with the analysis of the production of reactive oxygen species (ROS), CellROX® and in **Figure S7** with the quantification of activated microglia using methods for morpho-functional analysis described in, [141] respectively.

The secretion of pro-inflammatory cytokines and chemokine factors in mixed cell populations cultured on all experimental and control groups is presented in **Figure 6**. It is interesting to note that even though there is a linear increase in the release profile of IFN-γ in mixed cultures exposed to inflamed control conditions and when cultured on flattened PEDOT:PTS coated electrodes over time, Pt electrodes and pristine PEDOT:PTS coated electrodes followed a trend over time that was similar and constant, with no statistical differences noted between the expression profile of IFN-γ at day three and day ten respectively (Figure 6A). Importantly, the

lowest release profile of IFN-γ was observed with the micro-topographically functionalized PEDOT:PTS coated electrodes, with a maintained overall low and statistically significant release of this cytokine relative to all experimental and control groups by day ten. This cytokine is reportedly a crucial immunological player as it regulates relevant genes for cell function and cell programming. [141] Studies have shown that IFN-γ has a unique action on astrocytes, inducing pro-inflammatory activities and enhancing astrocyte-immunoreactivity. [139, 142] In a similar manner, TNF-α cytokine is known to act in synergy with IFN-γ, [143] showing a similar release trend on day seven and day ten respectively relative to the release profiles of IFN-γ on these days (Figure 6B). Over time, a linear decrease in TNF-α release was observed in all groups and controls, except for on the inflamed control group that presented a consistently high release profile of TNF-α. By day ten, a significantly higher release profile of TNF-α was observed in the inflamed control group which was comparable to that observed in VM cells cultured on flattened PEDOT:PTS coated electrodes. Control Pt, pristine PEDOT:PTS and micro-topographically functionalized PEDOT:PTS groups, were associated with a significant reduction in TNF-α synthesis and cells cultured on topographically functionalized PEDOT:PTS coated electrodes produced significantly less TNF-α than Pt control and other PEDOT:PTS experimental groups. These results indicate an activated response from astrocytes and microglia respectively, with their coordinated involvement in the host response at the material interface. [139, 143] Furthermore, the micro-pit topography utilized here also induced a reduced glial cell inflammatory response via CXCL-1, also known as KC/GRO (Figure 6C). CXCL-1 is associated with neutrophil recruitment, to a site of inflammation, [144] and a study by Rubio and colleagues [145] showed that astrocytes, as an early cell component of the neuro-immune response, produced CXCL-1 in the chemoattraction of the neutrophils and monocytes in neuro-inflammatory diseases. In this work, it was observed that by day ten, in contrast to a relatively high release profile of CXCL-1 from the inflammatory control conditions, an overall

significantly lower release response of CXCL-1 was exhibited by VM populations cultured on the micro-topographically PEDOT:PTS functionalized electrodes, a response maintained up to day ten in culture.

In primary mixed cultures, such as in the VM cells used in this research, as a consequence of the orchestrated release of cytokines and growth factors in neuronal-glial interactions, [139] there is a synergistic effect that allows them to work as co-stimulatory molecules to potentiate immune interactions, in this case at the local neuron-glial unit, with a resulting increase of specific cytokines response such as IL-6. [138, 139, 145]

At day three (Figure 6D), IL-6, which plays a vital role in immune regulation and is produced by astrocytes, microglia and neurons in injury-inflamed milieu, [146-150] showed a significantly potentiated release profile in the inflammatory control group, relative to an observed significant linear decrease in the release profile in VM cells cultured on all control and experimental electrode substrates. On day seven, comparatively significant increases in the release levels of IL-6 were observed on pristine and micro-topographically functionalized PEDOT:PTS electrodes relative to day three on bare platinum electrodes, flattened PEDOT:PTS coated electrodes and on the inflamed control, with significantly lower levels of IL-6 released VM cells cultured on micro-topographically functionalized PEDOT:PTS electrodes, maintained up to day ten.

Similar trends in the expression levels of IL-5 were also observed **(**Figure 6E), an important and often overlooked pro-inflammatory cytokine that has been shown to be produced by astrocytes and microglia *in vitro.* [138, 149] Further, IL-5 has been shown to induce nerve growth factor (NGF) secretion by astrocytes. [151-153] Again, the released IL-5 concentrations from micro-topographically functionalized PEDOT:PTS coated electrodes showed significant lower release profiles when compared to all groups, controls and inflamed control respectively at all time points.

Cytokines protein interactions adopting a confidence score >0.7 as the threshold to assess associations was performed and are detailed in **Figure S8**. These results suggest that the cytokine expression profiles observed from VM cells cultured on micro-topographically functionalized electrodes supports an overall neural-glial interaction at the electrode, associated with minimized reactive gliosis over time. [154] Indeed, this work has shown experimentally that the micro-topographically functionalized PEDOT:PTS coated electrodes here developed reduced the cytokine mechanisms of astrogliosis *in vitro*. This response was accentuated relative to bare platinum electrodes and pristine PEDOT:PTS coated electrodes, but further stressed when compared to flattened PEDOT:PTS coated electrodes, which resulted in the promotion of a more pro-inflammatory cytokine release and chemokine factors, reflected in the poor VM cell viability and outgrowth.

To evaluate the neuronal network activity and functionality of the neuronal population interfaced on topographically functionalized electrodes, further studies were conducted with mature explanted primary rat hippocampal neurons, which unlike embryonic VM populations, present functional neuronal network after seven to ten days in culture offering an important advantage to embryonic cells in terms of culture times.[155] Rat hippocampal cells were seeded on bare platinum electrodes, pristine PEDOT:PTS and on the micro-topographically functionalized PEDOT:PTS coated electrodes. Flattened PEDOT:PTS coated electrodes were not further evaluated due to the significant decrease in neuronal presence observed throughout the study.

Rat hippocampal cells successfully adhered and matured in all substrates and were analyzed after eight to ten days *in vitro* (three series of different cultures each), shown previously to be sufficient time to facilitate functional synaptic network development *in vitro* with matured explants. [156–158]

The formation of active synaptic networks was investigated by simultaneously imaging the intracellular calcium activity of living neurons (ten days *in vitro*) on representative regions of 660 x 660 µm. Neurons stained with the membrane permeable Ca^{2+} dye Oregon Green 488 BAPTA-1 were visualized within the sampled area and 8 ± 2 fluorescent cells were selected (regions of interest, ROIs) in each field (n = 25 fields) as in **Figure S9**A. At ten days *in vitro* matured neurons are synaptically connected and display spontaneous activity including bursts which manifest as irregular synchronized firing epochs.[159] This can be appreciated in Figure S9B, where two representative traces from region of interest (ROIs) in the same field are shown for each condition. The spontaneous bursting activity was fully blocked by TTX (1 µM; not shown) application, thus confirming the neuronal nature of the recorded signal. [159] The occurrence of spontaneous Ca^{2+} episodes in active cells was measured by quantifying the inter-event-interval (IEI). IEIs distribution was found to be different in the PEDOT:PTS-interfaced neuronal cultures (pristine and micro-patterned electrodes) when compared to those grown onto bare platinum electrodes (**$p < 0.01$; box plot in Figure S9C) suggesting a different coupling of the network with the substrate. However, median IEI values were comparable, being nine seconds and ten seconds for pristine PEDOT:PTS and micro-topographically functionalized PEDOT:PTS, respectively, and nine seconds for platinum (Figure S9C). The tested electrodes demonstrated a good cytocompatibility promoting functional hippocampal neurons development and allowing synaptogenesis and active network formation. In the presence of PEDOT:PTS coatings, neuronal activity appeared to be more organized into regular bursts and it may suggest that these might be related to the generation of a more favorable environment for neuronal activity. In turn, it was evident by the neuronal and astrocyte phenotypes visualized by immunofluorescence image of the specific cytoskeletal component, β-tubulin III, to visualize neurons, and glial fibrillary acidic protein (GFAP) to visualize astrocytes (**Figure S10**A) that a higher neuronal density was present on micro-topographically functionalized PEDOT:PTS coated electrodes. In addition, a decrease in the astrocyte-to-neuron ratio, was observed on

functionalized electrodes relative to bare platinum or pristine PEDOT:PTS electrodes (0.47 ± 0.16 versus 0.73 ± 0.34 and 0.68 ± 0.26 for bare platinum and pristine PEDOT:PTS controls respectively, ***$p < 0.001$ and **$p < 0.01$). These findings indicate that micro-topographically functionalized PEDOT:PTS coated electrodes promote the development of a non-reactive adherent glia network which promotes neuron-electrode interaction. Therefore, the possibility to exploit micro-topographically engineered PEDOT:PTS electrodes for neural interfacing and astrogliosis modulation is here strengthened.

3. Conclusion

The paradigm of neuroelectrode functionalization is the maintenance of electrode functionality and a controlled inflammatory response.[160, 161] Micro-pit topographical functionalized PEDOT:PTS coated electrodes were assessed for the first time as a methodology for the design of functionalized neural interface materials with a focus on reduced astrocyte reactive phenotype, enhanced neural integration and functional capacity.

Topographical functionalized PEDOT:PTS electrodes induced a significant reduction in electrical impedance and an increase in charge storage capacity and effective surface area, while maintaining electrode stability. Furthermore, the role of the micro-topographically modified PEDOT:PTS coated electrodes in reducing the characteristic phenotype associated with astrogliosis in complex primary mixed cell cultures was assessed from the evident morphological changes in cell area, the functional promotion of neural network activity, focal adhesion formation, and the release of pro-inflammatory cytokines and chemokine factors.

A low temperature imprint-lithography technique developed in this study for the micro-topographically functionalized neuroelectrode interfaces provides a useful bench-mark for subsequent studies with neural microelectrodes, and the development of dual functionalization with biological molecules on as-formed conducting polymer coatings. Furthermore, this work could shift the focus on current efforts in the field to attract astrocytes onto the electrode surface, but potentially blocking the negative components found in the glial cell response, *in vitro*.

4. Experimental section

4.1. Fabrication of Microelectrode Arrays

Ultra-short laser operating at 10 kHz and 1030 nm wavelength with 500 fs pulses duration was used to generate a microelectrode shadow mask in a Polyimide film of 0.05 mm thickness. Polyimide samples were placed on a 3D computer controlled stage (Aerotech) which enabled changes in the sample position with micrometer accuracy. The laser was focused on the sample with a 100 mm focal length lens and the scanning system was coupled to the machining stage through combination of different reflectors and mirrors. The laser spot diameter was found to be 25 µm and ablation threshold 0.56 Jcm^{-2}. To avoid the melting of Polyimide, a laser fluence of 0.6 Jcm^{-2} just above the threshold and 200 laser scans were used in drawing the electrode circuit design through the Polyimide film.

Through-mask sputtering of platinum was achieved with a EMSCOPE SC500 at 25 mA for twenty minutes. Resulting platinum electrode thickness was measured to be 69.27 nm ± 0.01 and resulted in an electrode size of 287.67 ± 0.08 µm in width.

4.2. Imprinting and Die Fabrication

Micro-topographically functionalized PEDOT:PTS coated electrode were made in a three-step process of photo-lithography, nickel die fabrication, and temperature low imprinting process.

4.2.1 Photo Lithography

100 mm diameter silicon-wafers were first cleaned using the [ozone / DI-water / dilute-HF acid] cleaning process on a Semitool SAT spray-acid cleaning-tool. The wafers were then coated with photoresist (Fujifilm HiPR6512) and the mask pattern exposed on an Ultratech 1500 stepper, after which the photoresist was developed using Fujifilm OPD5262 developer. A number of different masks were used to give various diameter patterns. The wafers were then dry-etched to the required depth for each pattern using a [SF6 / C_4F_8] plasma on an STS-ASE dry-etch tool. After dry-etching, the photoresist was removed by a combination of O_2 plasma ashing plus Piranha (H_2SO_4 / H_2O_2] wet-strip.

4.2.2 Nickel Die

This technique has been described previously. [51, 52] Briefly, nickel dies were made directly from the patterned resist samples. A thin (50-nm) layer of Ni-V was sputter coated on the samples. That layer acted as an electrode in the subsequent electroplating process. The dies were plated to a thickness of ca. 300 nm. For more information about the procedure, see reference [163]

4.2.3 Imprinting Process

PEDOT:PTS coated electrodes were imprinted by a low temperature imprinting process. Before the imprinting, the processed nickel die master was cut into 1 cm × 1 cm pieces, each piece acting as an individual stamp. The polymeric PEDOT:PTS coated electrodes were placed in a desiccator 24 hours prior to the imprinting process and then taken one by one to be processed. Using a hydraulic press machine (Carver, Inc), the nickel die stamp was then pressed against the PEDOT:PTS coated electrode, previously placed on pressing paralleled plates, using a compressive force of 1.9 metric tons cm^{-2} for fifteen minutes at room temperature.

Flattened controlled non-patterned PEDOT:PTS coated electrodes were processed by pressing a thick mirror glass stamps against the PEDOT:PTS coated electrode, applying a compressive force of 1.9 metric tons cm^{-2} for fifteen minutes at room temperature.

4.3. Physical Characterization

4.3.1 Surface Morphology

Scanning electron microscopy (SEM) was carried out using a Hitachi S-4700 Cold Field Emission Gun Scanning Electron Microscope (CFE-SEM). The SEM images were taken using an accelerating voltage of 15 kV and spot current of 10 µA. No gold sputtering was used on the conducting PEDOT:PTS coated electrodes.

Scanning electron microscopy for biological samples was carried out using a Hitachi S-4700 Cold Field Emission Gun Scanning Electron Microscope (CFE-SEM). Cells on experimental electrodes were stabilized in 4% paraformaldehyde with 1% sucrose in 0.1 M piperazine-N,N′-bis(2-ethanesulfonic acid) (PIPES) buffer at pH 7.4 for five minutes. Further, samples were

fixed permanently in 2.5% glutaraldehyde for five minutes in PIPES buffer and rinsed three times for two minutes in PIPES buffer. Additional contrasting of the cell was accomplished by staining with 1% osmium tetroxide in PIPES for one hour at 22°C and then rinsed in distilled water for one minute. After this, cells on experimental electrodes were dehydrated through an ethanol/distilled water series (50, 60, 70, 80, 90, 96 and 100%) followed by a hexamethyldisilazane (HDMS) or Acetone/Ethanol series (25, 50, 75 and 100 %). The samples were then left to dry fully and mounted on aluminium stubs, and coated with 10nm layer of gold (Au).

For surface 3D plots and roughness analysis, Atomic Force Microscopy (AFM) was performed as detailed in [7] All measurements were taken on a Vico Dimension 3100 AFM using TESPA Tips (NanoWorld) (Si <8 nm tip radius, 42 N/m spring constant, 320 kHz nominal resonance frequency), in tapping mode over an area of 10 μm^2 with a 0.5 - 1 Hz scan rate.

4.3.2 Thickness Measurements

The thickness of the polymeric PEDOT:PTS coating was measured using a Zygo Newview 100 surface profilometer controlled by MicroPlus software as detailed in [7] Briefly, a pattern of bright and dark lines - fringes was created as incoming light was split from the limited region between the sample film and the bare platinum electrode. This pattern difference was translated to calculate the height information, resulting in the thickness of the polymeric coatings.

4.4. Chemical Characterization

X-ray photoelectron spectroscopy (XPS) spectra were acquired on a Kratos AXIS 165 spectrometer XPS system with X-Ray Gun mono Al Kα 1486.58 eV; 150 W (10 mA, 15kV), for all scans with the following parameters: sample temperature in a range of 20-30 °C with a pass energy of 160 eV for survey spectra and 20 eV for narrow regions and steps of 1 eV for survey and 0.05 eV for regions with dwell times of 50 ms and 100 ms for regions and sweeps for survey of ~35, and for narrow regions of 6-40. The C1s line at 284.8 eV was used as charge reference. Spectra were collected in the normal way to the surface direction with an analysis

area of 60 microns. XPS detection limit is estimated to be ~0.1 at%. For the data processing, the construction and peak fitting of synthetic peaks in narrow region spectra was done using a Shirely type background and the synthetic peaks were of a mixed Gaussian-Lorenzian type. Relative sensitivity factors used are from CasaXPS library containing Scofield cross-sections.

4.5. Electrochemical Characterization

4.5.1 Preparation of PEDOT:PTS Samples

The electrodeposition of PEDOT:PTS coatings was conducted under ambient conditions according to methods described previously[164] Briefly, a solution of 0.05M EDOT (Sigma Aldrich, Ireland) and 0.1 M PTS (Sigma Aldrich, Ireland, 70,000 g/mol MW) was prepared in a 50/50 vol.% mixture of acetonitrile and water. The electrolyte solution was placed in an in-house fabricated electrochemical cell, connected to a Princeton Applied Research Potentiostat/Galvanostat model 2273 controlled with Power Suite software. An in- house-fabricated platinum microelectrode probe array and a platinum foil (Goodfellow) were used as the working electrode (WE) and counter-electrode (CE) respectively. A saturated 3 M KCl Ag/AgCl reference electrode (RE) (Bioanalytical Systems) was employed. Galvanostatic electrodeposition was performed and the efficiency of coating, i.e. the amount of polymer deposited on the electrodes, was controlled by the total charge passing during the electrodeposition. When the deposition was finalized, the coated electrodes were soaked in deionized water for 24 hours to remove excess of electrolyte and subsequently dried for use. For cell studies, PEDOT:PTS was electrodeposited on electrodes with areas of 1.6 cm^2 to facilitate *in vitro* manipulations.

4.5.2 Electrochemical Measurements

Cyclic voltammetry was performed as previously described in [7] using a Princeton Applied Research Potentiostat/Galvanostat model 2273 running with Power Suite software. Measurements were recorded in a custom-made electrochemical cell containing the microelectrode as working electrode, an Ag/AgCl reference electrode (3 M KCl) (Bioanalytical

Systems) and a platinum foil counter electrode (Goodfellow) in 1X phosphate-buffered saline (PBS). Cyclic voltammograms (CVs) were run in the potential range from -1.0 V to 0.4 V at a scan rate of 0.1 V s^{-1}. The charge storage capacity (CSC) was calculated by integrating the area enclosed by the voltammogram.

Electrical impedance spectroscopy (EIS) was performed using a Princeton Applied Research Potentiostat/Galvanostat model 2273 running with Power Suite software with a three-electrode set-up. The measurements were carried out in a frequency range of 0.1 Hz to 100 kHz with an AC sine wave of 40 mV amplitude applied with 0 V DC offset. The results were presented on Bode and Nyquist plots and compared to those of bare platinum microelectrodes and coated gold microelectrodes, to exclude the effect of electrode thickness when compared to PEDOT:PTS coated microelectrodes. The data fitting analysis was performed using EIS Spectrum Analyzer 1.0 software with the application of the Powell algorithm.

Electroactive surface area (ESA) measurements for each microelectrode were done through cyclic voltammetry scans performed in 2.5 mol cm-3 K4[Fe(CN)6] 0.1 M KCl solution, in the potential range from -1.0 V to 0.4 V at a scan rate of 0.1 V s^{-1}. ESA was estimated according to the Randles-Sevcik equation:[165, 166]

$$i_p = 2.69 \cdot 10^5 A D^{1/2} n^{3/2} \upsilon^{1/2} C \qquad \textbf{Equation 1}$$

where i_p is the reduction/oxidation peak current (A), n is the number of electrons contributing to the redox reaction, A is the area of the electrode (cm^{-2}), D is the diffusion coefficient of $Fe(CN)_6^{4-}$ in KCl solution ($6.3 \cdot 10^{-6}$ cm^2 s^{-1}), [167] C is the concentration of the $Fe(CN)_6^{4-}$ in the bulk solution (mol cm^{-3}) and υ is the scan rate (V s^{-1}). The measurements were performed in triplicate; the results were expressed as a mean ± standard deviation.

The electrochemical stability of microelectrodes was determined as described previously in [8] Briefly, cyclic voltammetry was performed before and after electrical stability measurements and used to calculate the percentage of loss in charge storage capacity by comparing the CSC

of the 1st and 500th cycles. The measurements were performed in triplicate; the results were expressed as a mean ± standard deviation.

Force-controlled current-voltage (I-V) characteristics were recorded employing conductive-AFM (C-AFM) (in PeakForce Tuna mode, PF Tuna, Bruker). Samples were imaged under ambient conditions with a Bruker Dimension Icon microscope, with a NanoScope IV control unit and PF-TUNA add-on module. One sapphire substrate with gold contact was used to connect samples to form the electric circuit. I-V curves were recorded at selective positions on the sample surface. C-AFM tips (coated with Platinum/Iridium) were used as the mobile counter electrode to contact the single-walled carbon nanotubes – (SWCNTs) PeakForce-TUNA tips, Bruker. For a schematic of the set-up, see Figure S4. The voltage bias was ramped between -500mV and 500mV. The data was then analyzed by NanoScope Analysis (version 1.5, Bruker) and Matlab (version 2016 a).

4.6. Biological Characterization

4.6.1 Cell Culture

Primary cultures of ventral mesencephalic neurons (VM) were obtained from the mesencephalon of embryonic Sprague–Dawley rats according to methods previously described by Vallejo-Giraldo et al. [7] Briefly, the ventral mesencephalon were dissected from embryonic fourteen-day rat brains and then mechanically dissociated with a pipette until the tissue was dispersed. Cells were grown in a humidified atmosphere of 5% CO_2 at 37°C and culture in media (Dulbecco's modified Eagle's medium/F12, 33 mM D-glucose, 1 % L-glutamine, 1% penicillin-streptomycin (PS), 1 % fetal calf serum (FCS), supplemented with 2 % B27). Controls and experimental groups were cultured for three, seven and ten days in six well culture plates and sterilized in 70% ethanol for two hours, and subsequently washed repeatedly with hank's balanced salt solution (HBSS) and/or molecular biology grade water (Sigma). Prior to plating, samples and controls were coated with poly-lysine (PLL) (Sigma). They were then rinsed three times with molecular biology grade water and left to dry overnight. 50,000 cells

cm^{-2} were plated on each electrode, and then 3 ml of the culture medium was added to each well and half of the volume was replaced with fresh media every two days for a period of ten days.

For the inflammatory control, primary VM cells were cultured on sterile Thermanox® Plastic Coverslips with 13 mm diameter (NUNCTM brand products). 50,000 cells cm^{-2} were plated on each coverslip, and grown in a humidified atmosphere of 5% CO_2 at 37°C and culture in media (Dulbecco's modified Eagle's medium/F12, 33 mM D-glucose, 1 % L-glutamine, 1% PS, 1 % FCS, supplemented with 2 % B27). 3 ml of the culture medium was added to each well and, after two days in culture, the cells were stimulated with IL-1β (10 ng mL^{-1}) prepared in plating media to a final volume of 3 ml and half of the volume was changed every two days for a period of ten days. Data for the optimization of the different concentration of IL-1β as inflammatory stimuli on VM cells cultures is shown in **Figure S6** with the analysis of the production of reactive oxygen species (ROS), CellROX® and in **Figure S7** with the quantification of activated microglia using methods for morpho-functional analysis described in [141] respectively. Dissociated hippocampal neurons were obtained from P1 to P4-old Wistar rats as previously reported.[156] Prior to plating, samples of pristine PEDOT:PTS and micro-topographically functionalized PEDOT:PTS coated electrodes and control bare platinum were sterilized by repeated (three) ten minutes-long washes with ethanol followed by five minutes-long washes in molecular biology grade water, both solutions were previously filtered with 0.22 µm cutoff filter (Merck Millipore). Cultured cells were incubated at 37 °C, 5 % CO_2 in culture medium composed of Neurobasal-A (Thermo Fischer) containing B27 2 % (Gibco) Glutamax 10 mM and Gentamycin 0.5 µM (Gibco), and used for experiments at eight–ten days *in vitro* by renewing half of the medium once in this period.

Ethical Statement (Primary hippocampal cultures)

All experiments were performed in accordance with the EU guidelines (2010/63/UE) and Italian law (decree 26/14) and were approved by the local authority veterinary service and by our

institution (SISSA-ISAS) ethical committee. Every effort was made to minimize animal suffering and to reduce the number of animals used. Animal use was approved by the Italian Ministry of Health, in accordance with the EU Recommendation 2007/526/CE.

4.6.2 Immunofluorescent Labeling

Indirect double-immunofluorescent labeling was performed to visualize neurons and astrocyte cell populations as described by Vallejo-Giraldo et al. [8] Briefly, VM cells on experimental and control substrates were fixed with 4% paraformaldehyde and 1% of sucrose for twenty minutes at room temperature at the time point. Once fixed, the samples were washed with PBS and permeabilized with buffered 0.5% Triton X-100 within a buffered isotonic solution (10.3 g sucrose, 0.292 g NaCl, 0.06 g $MgCl_2$, 0.476 g HEPES buffer, 0.5 ml Triton X-100, in 100 ml water, pH 7.2) at 4ºC for five minutes. Non-specific binding sites were blocked with 1% bovine serum albumin (BSA) in PBS at 37ºC for 30 minutes and subsequently incubated for two hours with a 1:200 concentration anti-glial fibrillary acidic protein (GFAP) antibody produced in mouse (Sigma, 1:200) and 1:500 concentration anti-β-Tubulin III antibody produced in rabbit (Sigma, 1:500). Samples were washed three times with 0.05% Tween 20/PBS and then incubated for one hour in the secondary antibody Alexa Fluor® 488 goat anti-Mouse IgG / IgA / IgM (H+L) (Molecular probes 1:500) combined with the secondary antibody Alexa Fluor® 594 goat anti-Rabbit IgG (H+L) (Molecular probes, 1:500). Samples were washed with PBS (five minutes ×3) and mounted on microscope cover slides and counterstained with slowfadeR gold antifade reagent with DAPI for nuclear staining.

Indirect double-immunofluorescent labeling was performed to visualize focal adhesion sites and astrocytes following the fixation and permeabilization processes detailed above. In this case the samples were incubated for two hours with a 1:200 concentration anti-Paxillian (Rb mAb to Paxillin (Y113) (Life Technologies, 1:200) and with a 1:200 concentration GFAP antibody produced in mouse (Sigma, 1:200). Samples were washed three times with 0.05% Tween 20/PBS and then incubated for one hour in the secondary antibody Alexa Fluor® 488 goat anti-

Mouse IgG / IgA / IgM (H+L) (Molecular probes 1:500) combined with the secondary antibody Alexa Fluor® 594 goat anti-Rabbit IgG (H+L) (Molecular probes, 1:100). Samples were washed with PBS (five minutes ×3) and mounted on microscope cover slides and counterstained with slowfadeR gold antifade reagent with DAPI for nuclear staining.

Indirect double-immunofluorescent labeling for microglia and astrocytes on inflamed controls was performed using the same methods detailed above. Samples were incubated for two hours with GFAP antibody produced in mouse (Sigma, 1:200) at a concentration of 1:200 and with anti-rabbit Iba1 (Wako, 1:1000) with a concentration of 1:1000. Samples were washed three times with 0.05% Tween 20/PBS and then incubated for one hour in the secondary antibody Alexa Fluor® 488 goat anti-Mouse IgG / IgA / IgM (H+L) (Molecular probes 1:500) combined with the secondary antibody Alexa Fluor® 594 goat anti-Rabbit IgG (H+L) (Molecular probes, 1:1000). Samples were washed with PBS (five minutes ×3) and mounted on microscope cover slides and counterstained with slowfadeR gold antifade reagent with DAPI for nuclear staining.

Hippocampal dissociated cultures were fixed in 4% formaldehyde (prepared from fresh paraformaldehyde) in PBS and permeabilized for twenty min with 0.3% Triton-X-100 (Carlo Erba) in PBS added with 5% FCS (Gibco) and 4% BSA (Sigma-Aldrich) to prevent non-specific binding of primary antibodies. Samples were subsequently incubated with primary antibodies for 30 minutes at room temperature and, after being washed with PBS, with secondary antibodies for 45 minutes. Mounting was performed with anti-fade medium Vectashield (Vector Laboratories) on 1 mm thick microscope glass slides. Neurons were labeled through anti-β-tubulin III primary antibody (Sigma-Aldrich T2200, 1:300) and visualized with Alexa 594 anti-rabbit in goat as secondary antibody (Invitrogen, 1:500). Astrocytes were stained with mouse anti-GFAP primary antibodies (Sigma-Aldrich G3893, 1:300) and visualized with Alexa 488 anti-mouse in goat as secondary antibody (Invitrogen 1:500). Nuclei were stained with 4',6-diamidino-2-phenylindole (DAPI, Invitrogen, 1:500).

The production of reactive oxygen species (ROS) on inflamed controls was visualized using an assay kit, CellROX® Green Reagent, for oxidative stress detection (2.5 mM; Thermo Fisher Scientific - C10444). CellROX® Green Reagent was diluted in HBSS for a final concentration of 5 µM (working solution) that was prepared fresh every time used. During use, this working solution was kept in the dark at 37 °C. After removing cell media, CellROX® Green Reagent was added on each sample and incubated at 37 °C for 30 minutes. After incubation, each sample was fixed and permeabilized using methods described aboved. One hour incubation in rhodamine-conjugated phalloidin (Life Techologies, 1:100) prepared in 1% BSA in PBS was followed next for F-actin staining. After being washed with PBS (five minutes ×3), samples were mounted with slowfadeR gold antifade reagent with DAPI for nuclear staining and image within 24 hours. CellROX® Green was visualized using FTIC channel.

4.6.3 Microscopy and Image Analysis

After immunostaining, samples were viewed with an Olympus Fluoview 1000 Confocal Microscope at a fixed scan size of 1024 by 1024 at a ratio 1:1. Cell analysis was performed as described in [8] At least twenty images at 60× magnification were taken at random from each experimental group and controls. Cell density was analyzed by counting the total number of labeled nuclei corresponding to neurons and astrocytes in an area of 212 µm * 212 µm. Neurite length was quantified by analyzing nine random fields of view of three different technical replicas from three different samples using established stereological methods. [69] The formula used was: neurite length = n*T *π/2, where n is the number of times neurites intersect grid lines and T = distance between gridlines (taking magnification into account) as described in [168] Cell area of astrocytes was recorded from the green channel using the threshold function to generate particles that were manually dispersed across the image until good coverage was achieved. The total number of focal adhesion points per cell and their length were quantified by direct scoring with a four pixel-wide line on the FITC channel as previously described in [7] using ImageJ software (National Institutes of Health, USA).

Images of immunolabeled hippocampal dissociated cultures were acquired using a Leica DM6000 Epifluorescence Microscope either at 10× or 20× magnification (dry objectives, and 0.5 NA respectively). Eight fields per culture from three different culture series were collected. In addition, a Nikon C2 confocal microscope was used to acquire higher quality images at 40× magnification (dry objective) to obtain a morphological insight of stained cells. Analysis and images reconstruction were accomplished using NIS-Elements AR (Nikon), Velocity (PerkinElmer) and ImageJ (NIH) software.

4.6.4 Cytokine Inflammatory Panel

The cytokine multiplex assay was performed on primary VM cell mixed population supernatants collected at three, seven and ten days in culture grown on all experimental groups, controls and inflamed control. ELISA pro-inflammatory panel 2 (Rat) (Meso Scale Discovery, UK) cytokine (IL-6, IL-1β, TNF-α, IFN-Y, KC/GRO, IL-4, IL-5, IL-13, IL-10) assays were performed according to the manufacturer's instructions, using six replicas and without adjustments to the recommended standard curve, and sample dilutions. Briefly, 150 µL of blocker H was added on each well of ELISA pro-inflammatory plate and incubated at room temperature with fast shaking for one hour. In parallel, in a separate provided plate, an initial 1:2 dilution of samples and culture media was prepared and put under shaking for fifteen minutes. The ELISA pro-inflammatory plate was then washed three times with at least 150 µL of wash buffer (PBS with 0.05% Tween20) and subsequently, the diluted sample mixed from the additional plate provided was transferred to the ELISA pro-inflammatory plate with the addition of 25 µl of diluent 40. Incubation at room temperature with shaking for two hours was then carried out. The ELISA pro-inflammatory plate was further washed three times with PBS-tween20, and 25 µL of 1X detection antibody solution was added in each well and incubated at room temperature with shaking for two hours. The ELISA pro-inflammatory plate was washed three times and further added 150 µL of 2X read buffer T in each well for plate reading using the QuickPlex SQ 120 multiplexing instrument from MSD.

The STRING (search Tool for the Retrieval of Interacting Genes) database http://string-db.org search was performed for known protein interactions adopting a confidence score >0.7 as the threshold to assess associations.

4.7. Calcium Imaging

Hippocampal dissociated cultures were loaded with cell permeable Ca^{2+} dye Oregon Green 488 BAPTA-1 AM (Molecular Probes); 10 µL DMSO (Sigma-Aldrich) was added to the stock 50 µg of the dye and cultures were incubated with a final concentration of 4 µM for 30 minutes at 37 °C, 5% CO_2, as detailed previously in [7] Samples were thereafter placed in a recording chamber mounted on an inverted microscope (Nikon Eclipse Ti-U). Cultures were continuously perfused at 5 mL min^{-1} rate and at room temperature with extracellular solution of composition (mM): 150 NaCl, 4 KCl, 2 $CaCl_2$, 1 $MgCl_2$, 10 HEPES, 10 glucose (pH adjusted to 7.4 with NaOH; osmolarity 300 mOsm). Ca^{2+} dye was excited at 488 nm with a mercury lamp; excitation light was separated from the light emitted from the sample using a 395 nm dichroic mirror and ND filter (1/32). Oregon loaded cultures were observed with a 20× objective (0.45 NA PlanFluor) and images were continuously acquired (exposure time 150 ms) using an ORCA-Flash4.0 V2 sCMOS camera (Hamamatsu). The imaging system was controlled by an integrated imaging software (HCImage Live) and the camera was set to operate on 2048 × 2048 pixels at binning four. After eight minutes of spontaneous activity recording, 1 µM TTX (a voltage-gated, fast Na+ channel blocker; Latoxan) was added to confirm the neuronal nature of the recorded signals. Three fields from each sample (two samples per condition) were recorded and 8 ± 2 cells from each recording were selected by drawing regions of interest (ROIs) around cell bodies as depicted in Figure S9A. Images were analyzed with both ImageJ software (NIH) and Clampfit software (pClamp suite, 10.4 version; Axon Instruments) in off-line mode. [169] The difference between peaks consecutive onset times were computed, to obtain the inter-event interval (IEI). Intracellular Ca^{2+} transients were expressed as fractional amplitude increase ($\Delta F/F_0$, where F_0 is the baseline fluorescence level and ΔF is the rise over baseline); the onset

time of neuronal activation was determined by detecting those events in the fluorescence signal that exceed at least five times the standard deviation of the noise.

4.8. Statistical Analysis

All data presented here was confirmed using at least three replicates for each of the test groups and control groups. The results are expressed as the mean of the values ± standard error of the mean. One-way ANOVA followed by a Bonferroni test were performed to determine the statistical significance ($p<0.05$), unless otherwise stated.

Supporting Information

Supporting Information is available from the Wiley Online Library or from the author.

Acknowledgements

M.J. Biggs is also an SFI, Starting Investigator SIRG COFUND fellow, grant no. 11/SIRG/B2135. This grant was the principal funder of the research. This publication has also emanated from research supported in part by a research grant from Science Foundation Ireland (SFI) and is co-funded under the European Regional Development Fund under Grant Number 13/RC/2073. The authors would like to thank the following people: Ms Nuala Campbell and Ms Eugenia Pugliese for their help in cell quantification, Dr. Karrina McNamara and Dr. Tofail Syed for their help in XPS analysis.

The authors are grateful to the facilities and technical assistance of the NCBES Electron Microscopy unit within the Centre for Microscopy & Imaging at the National University of Ireland Galway, a facility that is funded by NUIG and the Irish Government's Programme for Research in Third Level Institutions, Cycles 4 and 5, National Development Plan 2007-2013 and also to the Genomics & Screening Core at the National University of Ireland Galway. The authors would like to acknowledge the Tyndall National Institute and the National Access Programme Grant Number NAP428 for preparation of nickel shims emanated from research conducted with the financial support of Science Foundation Ireland under Grant Number [SFI/04/CE/I590a7].

Received: ((will be filled in by the editorial staff))
Revised: ((will be filled in by the editorial staff))
Published online: ((will be filled in by the editorial staff))

References

[1] Lahr, J.; Schwartz, C.; Heimbach, B.; Aertsen, A.; Rickert, J.; Ball, T., *J. Neural Eng.* **2015**, 12 (4), 043001.

[2] Vanleer, A. C.; Blanco, J. A.; Wagenaar, J. B.; Viventi, J.; Contreras, D.; Litt, B., *J. Neural Eng.* **2016**, 13 (2), 026015.

[3] Fattahi, P.; Yang, G.; Kim, G.; Abidian, M. R., *Adv Mater* **2014**, 26 (12), 1846-1885.

[4] Durand, D. M.; Ghovanloo, M.; Krames, E., *J. Neural Eng.* **2014**, 11 (2), 020201.

[5] Zhou, Z.; Yu, P.; Geller, H. M.; Ober, C. K., *Biomacromolecules* **2013**, 14 (2), 529-537.

[6] Aregueta-Robles, U. A.; Woolley, A. J.; Poole-Warren, L. A.; Lovell, N. H.; Green, R. A., *Frontiers in Neuroengineering* **2014**, 7 (15).

[7] Vallejo-Giraldo, C.; N. P. P., Anuradha R. Pallipurath, John; O'Connell, J. D. H., Parvaneh Mokarian-Tabari, Alexandre Trotier, Katarzyna; Krukiewicz, G. O.-A., Eugenia Pugliese, Laura Ballerini, Michelle Kilcoyne,; Eilís Dowd, L. R. Q., Abhay Pandit, Paul Kavanagh and Manus Jonathan Paul; Biggs, *Adv Funct Mater* **2017**. DOI:10.1002/adfm.201605035

[8] Vallejo-Giraldo, C.; Pugliese, E.; Larranaga, A.; Fernandez-Yague, M. A.; Britton, J. J.; Trotier, A.; Tadayyon, G.; Kelly, A.; Rago, I.; Sarasua, J. R.; Dowd, E.; Quinlan, L. R.; Pandit, A.; Biggs, M. J., *Nanomedicine (Lond)* **2016**, 11 (19), 2547-63.

[9] Agnew, W. F.; McCreery, D. B., *Neural Prostheses: Fundamental Studies.* Prentice Hall: **1990.**

[10] Cogan, S. F., Annu. *Rev. Biomed. Eng*. **2008**, 10, 275-309.

[11] Rousche, P. J.; Pellinen, D. S.; Pivin, D. P., Jr.; Williams, J. C.; Vetter, R. J.; Kipke, D. R., *IEEE Trans Biomed Eng* **2001**, 48 (3), 361-71.

[12] Mantione, D.; Del Agua, I.; Schaafsma, W.; Diez-Garcia, J.; Castro, B.; Sardon, H.; Mecerreyes, D., *Macromol Biosci* **2016**, 16 (8), 1227-38.

[13] Boehler, C.; Stieglitz, T.; Asplund, M., *Biomaterials* **2015**, 67, 346-353.

[14] Chapman, C. A. R.; Chen, H.; Stamou, M.; Biener, J.; Biener, M. M.; Lein, P. J.; Seker, E., *ACS Appl Mater Interfaces* **2015**, 7 (13), 7093-7100.

[15] Asplund, M.; Nyberg, T.; Inganas, O., *Polym Chem-Uk* **2010**, 1 (9), 1374-1391.

[16] Green, R. A.; Baek, S.; Poole-Warren, L. A.; Martens, P. J., *Sci Technol Adv Mat* **2010**, 11 (1), 014107.

[17] Green, R. A.; Lovell, N. H.; Wallace, G. G.; Poole-Warren, L. A., *Biomaterials* **2008**, 29 (24), 3393-3399.

[18] Balint, R.; Cassidy, N. J.; Cartmell, S. H., *Acta Biomater* **2014**, 10 (6), 2341-2353.

[19] Mario Cheong, G. L.; Lim, K. S.; Jakubowicz, A.; Martens, P. J.; Poole-Warren, L. A.; Green, R. A., *Acta Biomater* **2014**, 10 (3), 1216-1226.

[20] Vallejo-Giraldo, C.; Kelly, A.; Biggs, M. J. P., *Drug Discov. Today* **2014**, 19 (1), 88-94.

[21] Shi, Y.; Pan, L.; Liu, B.; Wang, Y.; Cui, Y.; Bao, Z.; Yu, G., *Journal of Materials Chemistry A* **2014**, 2 (17), 6086-6091.

[22] Zhang, W.; Yang, F. K.; Pan, Z.; Zhang, J.; Zhao, B., *Macromol Rapid Commun* **2014**, 35 (3), 350-354.

[23] Xu, H.; Holzwarth, J. M.; Yan, Y.; Xu, P.; Zheng, H.; Yin, Y.; Li, S.; Ma, P. X., *Biomaterials* **2014**, 35 (1), 225-235.

[24] King, Z. A.; Shaw, C. M.; Spanninga, S. A.; Martin, D. C., *Polymer (Guildf)* **2011**, 52 (5), 1302-1308.

[25] Martin, D. C.; Wu, J.; Shaw, C. M.; King, Z.; Spanninga, S. A.; Richardson-Burns, S.; Hendricks, J.; Yang, J., *Polym. Rev. (Philadelphia, PA, U. S.)* **2010**, 50 (3), 340-384.

[26] Castagnola, V.; Descamps, E.; Lecestre, A.; Dahan, L.; Remaud, J.; Nowak, L. G.; Bergaud, C., *Biosens. Bioelectron*. **2015**, 67, 450-457.

[27] Wu, F.; Sun, M.; Jiang, W.; Zhang, K.; Xie, A.; Wang, Y.; Wang, M., *Journal of Materials Chemistry C* **2016**, 4 (1), 82-88.

[28] Xiao, H.; Zhang, M.; Xiao, Y.; Che, J., *Colloids and Surfaces B: Biointerfaces* **2015**, 126, 138-145.

[29] Fonner, J. M.; Forciniti, L.; Nguyen, H.; Byrne, J. D.; Kou, Y. F.; Syeda-Nawaz, J.; Schmidt, C. E., *Biomed Mater* **2008**, 3 (3), 034124.

[30] Cui, X.; Lee, V. A.; Raphael, Y.; Wiler, J. A.; Hetke, J. F.; Anderson, D. J.; Martin, D. C., *J Biomed Mater Res* **2001**, 56 (2), 261-72.

[31] Abidian, M. R.; Corey, J. M.; Kipke, D. R.; Martin, D. C., *Small* **2010,** 6 (3), 421-9.

[32] Wolfs, M.; Darmanin, T.; Guittard, F., *Surf. Coat. Technol.* **2014**, 259, 594-598.

[33] Culebras, M.; Gomez, C.; Cantarero, A., *Journal of Materials Chemistry A* **2014**, 2 (26), 10109-10115.

[34] Oyman, G.; Geyik, C.; Ayranci, R.; Ak, M.; Demirkol, D. O.; Timur, S.; Coskunol, H., *Rsc Adv* **2014**, 4 (96), 53411-53418.

[35] Zhu, Z.; Mankowski, T.; Balakrishnan, K.; Shikoh, A. S.; Touati, F.; Benammar, M. A.; Mansuripur, M.; Falco, C. M., ACS *Appl Mater Interfaces* **2015**, 7 (30), 16223-16230.

[36] Wei, B.; Liu, J.; Ouyang, L.; Kuo, C.-C.; Martin, D. C., *ACS Appl Mater Interfaces* **2015**, 7 (28), 15388-15394.

[37] Deng, H.; Lin, L.; Ji, M.; Zhang, S.; Yang, M.; Fu, Q., *Prog Polym Sci* **2014**, 39 (4), 627-655.

[38] Uppalapati, D.; Boyd, B. J.; Garg, S.; Travas-Sejdic, J.; Svirskis, D., *Biomaterials* **2016**, 111, 149-162.

[39] Vara, H.; Collazos-Castro, J. E., *ACS Appl Mater Interfaces* **2015**, 7 (48), 27016-27026.

[40] Kim, D. H.; Wiler, J. A.; Anderson, D. J.; Kipke, D. R.; Martin, D. C., *Acta Biomater* **2010**, 6 (1), 57-62.

[41] Asplund, M.; Thaning, E.; Lundberg, J.; Sandberg-Nordqvist, A. C.; Kostyszyn, B.; Inganas, O.; von Holst, H., *Biomed Mater* **2009**, 4 (4), 045009.

[42] George, P. M.; Lyckman, A. W.; LaVan, D. A.; Hegde, A.; Leung, Y.; Avasare, R.; Testa, C.; Alexander, P. M.; Langer, R.; Sur, M., *Biomaterials* **2005**, 26 (17), 3511-9.

[43] Pearce, T. M.; Williams, J. C., *Lab Chip* **2007**, 7 (1), 30-40.

[44] HajjHassan, M.; Chodavarapu, V.; Musallam, S., *Sensors* **2008**, 8 (10), 6704-6726.

[45] Donoghue, J. P., *Nat Neurosci* **2002**, 5, 1085-1088.

[46] Kotov, N. A.; Winter, J. O.; Clements, I. P.; Jan, E.; Timko, B. P.; Campidelli, S.; Pathak, S.; Mazzatenta, A.; Lieber, C. M.; Prato, M., *Adv Mater* **2009**, 21 (40), 3970-4004.

[47] Brüggemann, D.; Michael, K. E.; Wolfrum, B.; Offenhäusser, A., *International Journal of Nano and Biomaterials 17* **2012**, 4 (2), 108-127.

[48] Cui, X.; Hetke, J. F.; Wiler, J. A.; Anderson, D. J.; Martin, D. C., *Sensors and Actuators A: Physical* **2001**, 93 (1), 8-18.

[49] Asplund, M.; Nyberg, T.; Inganäs, O., *Polym Chem-Uk* **2010**, 1 (9), 1374-1391.

[50] Biggs, M. J. P.; Richards, R. G.; Dalby, M. J., *Nanomedicine: Nanotechnology, Biology and Medicine* **2010**, 6 (5), 619-633.

[51] Biggs, M. J.; Richards, R. G.; Gadegaard, N.; McMurray, R. J.; Affrossman, S.; Wilkinson, C. D.; Oreffo, R. O.; Dalby, M. J., *J Biomed Mater Res A* **2009,** 91 (1), 195-208.

[52] Biggs, M. J.; Richards, R.; Gadegaard, N.; Wilkinson, C.; Dalby, M., *J. Orthop. Res.* **2007**, 25 (2), 273-282.

[53] Morgan, J. T.; Murphy, C. J.; Russell, P., *Exp. Eye Res.* **2013**, 115, 1-12.

[54] Sofroniew, M. V., *Trends Neurosci.* **2009**, 32 (12), 638-647.

[55] Polikov, V. S.; Tresco, P. A.; Reichert, W. M., *J Neurosci Methods* **2005**, 148 (1), 1-18.

[56] Chapman, C. A.; Wang, L.; Chen, H.; Garrison, J.; Lein, P. J.; Seker, E., *Adv Funct Mater* **2016**.

[57] Ereifej, E. S.; Matthew, H. W.; Newaz, G.; Mukhopadhyay, A.; Auner, G.; Salakhutdinov, I.; VandeVord, P. J., *Journal of Biomedical Materials Research Part A* **2013**, 101 (6), 1743-1757.

[58] Tawil, N.; Wilson, P.; Carbonetto, S., *The Journal of Cell Biology* **1993**, 120 (1), 261-271.

[59] Biggs, M. J. P.; Dalby, M. J., *Proc Inst Mech Eng H* **2010**, 224 (12), 1441-1453.

[60] Turner, D. A.; Adamson, D. C., *J. Neuropathol. Exp. Neurol.* **2011**, 70 (3), 167-176.

[61] Turner, A. M.; Dowell, N.; Turner, S. W.; Kam, L.; Isaacson, M.; Turner, J. N.; Craighead, H. G.; Shain, W., *J Biomed Mater Res* **2000**, 51 (3), 430-41.

[62] Leber, M.; Shandhi, M.; Hogan, A.; Solzbacher, F.; Bhandari, R.; Negi, S., *Appl. Surf. Sci.* **2016**, 365, 180-190.

[63] Corey, J.; Wheeler, B.; Brewer, G., *IEEE Trans. Biomed. Eng.* **1996**, 43 (9), 944-955.

[64] Chung, C.-K.; Tseng, S.-F.; Hsiao, W.-T.; Chiang, D.; Lin, W.-C., *Journal of Laser Micro Nanoengineering* **2016**, 11 (3), 395-399.

[65] Thakar, R.; Weber, A. E.; Morris, C. A.; Baker, L. A., *Analyst* **2013**, 138 (20), 5973-82.

[66] Bass, R. B.; Clark, W. W.; Zhang, J. Z.; Lichtenberger, A. W., *IEEE Transactions on Applied Superconductivity* **2001**, 11 (1), 92-94.

[67] Moulin, E.; Bittkau, K.; Ghosh, M.; Bugnon, G.; Stuckelberger, M.; Meier, M.; Haug, F.-J.; Hüpkes, J.; Ballif, C., *Sol. Energy Mater. Sol. Cells* **2016**, 145, 185-192.

[68] Herth, E.; Algré, E.; Rauch, J. Y.; Gerbedoen, J. C.; Defrance, N.; Delobelle, P., *physica status solidi (a)* **2016**, 213 (1), 114-121.

[69] Khaldi, A.; Maziz, A.; Plesse, C.; Soyer, C.; Vidal, F.; Cattan, E., *Sensors and Actuators B: Chemical* **2016**, 229, 635-645.

[70] Li, Z.; Chen, Y.; Zhu, X.; Zheng, M.; Dong, F.; Chen, P.; Xu, L.; Chu, W.; Duan, H., *Nanotechnology* **2016**, 27 (36), 365302.

[71] Ma, S.; Xia, Y.; Wang, Y.; Ren, K.; Luo, R.; Song, L.; Chen, X.; Chen, J.; Jin, Y., *Journal of Vacuum Science & Technology B, Nanotechnology and Microelectronics: Materials, Processing, Measurement, and Phenomena* **2016**, 34 (5), 052002.

[72] Wulz, T.; Canfield, B. K.; Davis, L. M.; Spanier, S.; Lukosi, E., *Diamond Relat. Mater.* **2017**, 74, 108-113.

[73] Hof, L. A.; Guo, X.; Seo, M.; Wüthrich, R.; Greener, J., *Micromachines* **2017**, 8 (1), 29.

[74] Ereifej, E. S.; Cheng, M. M.-C.; Mao, G.; VandeVord, P. J., *J Neurosci Methods* **2013**, 217 (1), 17-25.

[75] Gomez, N.; Lee, J. Y.; Nickels, J. D.; Schmidt, C. E., *Adv Funct Mater* **2007**, 17 (10), 1645-1653.

[76] Hoshino, T.; Miyazako, H.; Nakayama, A.; Wagatsuma, A.; Mabuchi, K., *Sensors and Actuators B: Chemical* **2016**, 236, 659-667.

[77] Zhang, L.; Ducharme, S.; Li, J., *Appl. Phys. Lett.* **2007**, 91 (17), 172906.

[78] Chen, Y.; Ohlberg, D. A.; Li, X.; Stewart, D. R.; Stanley Williams, R.; Jeppesen, J. O.; Nielsen, K. A.; Stoddart, J. F.; Olynick, D. L.; Anderson, E., *Appl. Phys. Lett.* **2003**, 82 (10), 1610-1612.

[79] Jingfeng, S.; Haidong, L.; Shumin, L.; Li, T.; Alexei, G.; Stephen, D., *Nanotechnology* **2016**, 27 (1), 015302.

[80] Yang, Y.; Lee, K.; Mielczarek, K.; Hu, W.; Zakhidov, A., *Nanotechnology* **2011**, 22 (48), 485301.

[81] Hourdakis, E.; Nassiopoulou, A. G., IEEE Trans. Electron *Devices* **2016**, 63 (2), 746-750.

[82] Kim, J.; Wubs, K.; Bae, B.-S.; Kim, W. S., *Sci Technol Adv Mat* **2012**, 13 (3), 035004.

[83] Ferrari, A.; Cecchini, M.; Dhawan, A.; Micera, S.; Tonazzini, I.; Stabile, R.; Pisignano, D.; Beltram, F., *Nano Lett.* **2011**, 11 (2), 505-511.

[84] Franco, D.; Milde, F.; Klingauf, M.; Orsenigo, F.; Dejana, E.; Poulikakos, D.; Cecchini, M.; Koumoutsakos, P.; Ferrari, A.; Kurtcuoglu, V., *Biomaterials* **2013**, 34 (5), 1488-1497.

[85] Franco, D.; Klingauf, M.; Bednarzik, M.; Cecchini, M.; Kurtcuoglu, V.; Gobrecht, J.; Poulikakos, D.; Ferrari, A., *Soft Matter* **2011**, 7 (16), 7313-7324.

[86] Schift, H.; Saxer, S.; Park, S.; Padeste, C.; Pieles, U.; Gobrecht, J., *Nanotechnology* **2005**, 16 (5), S171.

[87] Tan, L.; Kong, Y.; Pang, S.; Yee, A., *Journal of Vacuum Science & Technology B: Microelectronics and Nanometer Structures Processing, Measurement, and Phenomena* **2004**, 22 (5), 2486-2492.

[88] Pisignano, D.; Persano, L.; Raganato, M. F.; Visconti, P.; Cingolani, R.; Barbarella, G.; Favaretto, L.; Gigli, G., *Adv Mater* **2004**, 16 (6), 525-529. 98.

[89] Collazos-Castro, J. E.; Hernández-Labrado, G. R.; Polo, J. L.; García-Rama, C., *Biomaterials* **2013**, 34 (14), 3603-3617.

[90] Bhagwat, N.; Murray, R. E.; Shah, S. I.; Kiick, K. L.; Martin, D. C., *Acta Biomater* **2016**, 41, 235-246.

[91] Alves-Sampaio, A.; García-Rama, C.; Collazos-Castro, J. E., *Biomaterials* **2016**, 89, 98-113.

[92] Kim, D. H.; Richardson-Burns, S. M.; Hendricks, J. L.; Sequera, C.; Martin, D. C., *Adv Funct Mater* **2007**, 17 (1), 79-86.

[93] Shuhua, X.; Ziyou, L.; Ling, Y.; Fei, W.; Sun, G., *Mediat. Inflamm.* **2012**, 2012, 102954. DOI 10.1155/2012/102954.

[94] Strunecka, A.; Blaylock, R. L.; Strunecky, O., *Journal of Applied Biomedicine* **2016**, 14 (3), 171-176.

[95] Donoso, M.; Méndez-Vilas, A.; Bruque, J.; González-Martin, M., *Int. Biodeterior. Biodegrad.* **2007**, 59 (3), 245-251.

[96] Krukiewicz, K.; Zak, J. K., *J. Mater. Sci.* **2014**, 49 (16), 5738-5745.

[97] Krukiewicz, K.; Jarosz, T.; Zak, J. K.; Lapkowski, M.; Ruszkowski, P.; Bobkiewicz-Kozlowska, T.; Bednarczyk-Cwynar, B., *Acta Biomater* **2015**, 19, 158-65.

[98] Rivnay, J., Leleux, P., Ferro, M., Sessolo, M., Williamson, A., Koutsouras, D.A., Khodagholy, D., Ramuz, M., Strakosas, X., Owens, R.M. and Benar, C., *Science advances*, **2015**, 1(4), e1400251.

[99] Ludwig, K. A.; Langhals, N. B.; Joseph, M. D.; Richardson-Burns, S. M.; Hendricks, J. L.; Kipke, D. R., *J. Neural Eng.* **2011**, 8 (1), 014001.

[100] Abidian, M. R.; Martin, D. C., *Biomaterials* **2008**, 29 (9), 1273-1283.

[101] Abidian, M. R.; Ludwig, K. A.; Marzullo, T. C.; Martin, D. C.; Kipke, D. R., *Adv Mater* **2009**, 21 (37), 3764-3770.

[102] Molina, A.; González, J.; Laborda, E.; Wang, Y.; Compton, R. G., *Phys Chem Chem Phys* **2011**, 13 (32), 14694-14704.

[103] Rehacek, V.; Hotovy, I.; Vojs, M.; Mika, F., *Microsystem Technologies* **2008**, 14 (4-5), 491-498.

[104] Lin, Z.; Ino, K.; Shiku, H.; Matsue, T., *Chem. Commun*. **2010**, 46 (4), 559-561.

[105] Orozco, J.; Fernández-Sánchez, C.; Jiménez-Jorquera, C., *Sensors* **2010**, 10 (1), 475-490.

[106] Olowu, R. A.; Arotiba, O.; Mailu, S. N.; Waryo, T. T.; Baker, P.; Iwuoha, E., *Sensors* **2010**, 10 (11), 9872-9890.

[107] Ma, X.; Yue, G.; Wu, J.; Lan, Z.; Lin, J.-Y., *Rsc Adv* **2015**, 5 (54), 43639-43647.

[108] Wei, W.; Song, Y.; Wang, L.; Zhang, S.; Luo, J.; Xu, S.; Cai, X., *Microsystems & Nanoengineering* **2015**, 1.

[109] Arcot Desai, S.; Gutekunst, C.-A.; Potter, S. M.; Gross, R. E., *Front. Neuroengineering* **2014**, 7, 16.

[110] Zhang, H.; Shih, J.; Zhu, J.; Kotov, N. A., *Nano Lett.* **2012**, 12 (7), 3391-3398.

[111] Mandal, H. S.; Knaack, G. L.; Charkhkar, H.; McHail, D. G.; Kastee, J. S.; Dumas, T. C.; Peixoto, N.; Rubinson, J. F.; Pancrazio, J. J., *Acta Biomater* **2014**, 10 (6), 2446-2454.

[112] Nikkhah, M.; Edalat, F.; Manoucheri, S.; Khademhosseini, A., *Biomaterials* **2012**, 33 (21), 5230-46.

[113] Cesca, F.; Limongi, T.; Accardo, A.; Rocchi, A.; Orlando, M.; Shalabaeva, V.; Di Fabrizio, E.; Benfenati, F., *Rsc Adv* **2014**, 4 (86), 45696-45702.

[114] Qi, L.; Li, N.; Huang, R.; Song, Q.; Wang, L.; Zhang, Q.; Su, R.; Kong, T.; Tang, M.; Cheng, G., *PLoS One* **2013**, 8 (3), e59022.

[115] Fan, C.; Wang, H.; Chen, D.; Cheng, X.; Xiong, K.; Luo, X.; Cao, Q., *Neural regeneration research* **2014**, 9 (2), 119.

[116] Sun, W.; Incitti, T.; Migliaresi, C.; Quattrone, A.; Casarosa, S.; Motta, A., *J Tissue Eng Regen Med* **2015**.

[117] Runge, M. B.; Dadsetan, M.; Baltrusaitis, J.; Ruesink, T.; Lu, L.; Windebank, A. J.; Yaszemski, M. J., *Biomacromolecules* **2010**, 11 (11), 2845-2853.

[118] Kang, G.; Borgens, R. B.; Cho, Y., *Langmuir* **2011**, 27 (10), 6179-6184.

[119] Shi, X.; Xiao, Y.; Xiao, H.; Harris, G.; Wang, T.; Che, J., *Colloids and Surfaces B: Biointerfaces* **2016**, 145, 768-776.

[120] Gottipati, M. K.; Kalinina, I.; Bekyarova, E.; Haddon, R. C.; Parpura, V., *Nano Lett.* **2012**, 12 (9), 4742-4747.

[121] Ben Haim, L.; Rowitch, D. H., *Nat Rev Neurosci* **2017**, 18 (1), 31-41.

[122] Sofroniew, M. V.; Vinters, H. V., *Acta Neuropathol.* **2010**, 119 (1), 7-35.

[123] Oberheim, N. A.; Goldman, S. A.; Nedergaard, M., *Astrocytes: Methods and Protocols* **2012**, 23-45.

[124] Beggs, H. E.; Schahin-Reed, D.; Zang, K.; Goebbels, S.; Nave, K. A.; Gorski, J.; Jones, K. R.; Sretavan, D.; Reichardt, L. F., *Neuron* **2003**, 40 (3), 501-14.

[125] Ramakers, G. J.; Moolenaar, W. H., *Exp Cell Res* **1998**, 245 (2), 252-62.

[126] Koyama, Y.; Yoshioka, Y.; Matsuda, T.; Baba, A., *Glia* **2003**, 43 (2), 185-9.

[127] Padmanabhan, J.; Clayton, D.; Shelanski, M. L., *J. Neurobiol.* **1999**, 39 (3), 407-22.

[128] Paco, S.; Hummel, M.; Plá, V.; Sumoy, L.; Aguado, F., *BMC Genomics* **2016**, 17 (1), 304.

[129] Montgomery, D. L., *Vet. Pathol.* **1994**, 31 (2), 145-67.

[130] Cregg, J. M.; DePaul, M. A.; Filous, A. R.; Lang, B. T.; Tran, A.; Silver, *J., Exp. Neurol.* **2014**, 0, 197-207.

[131] Gilmour, A. D.; Goding, J.; Poole-Warren, L. A.; Thomson, C. E.; Green, R.A. *In In vitro biological assessment of electrode materials for neural interfaces,* **2015** 7th International IEEE/EMBS Conference on Neural Engineering (NER), 22-24 April 2015; 2015; pp 450-453.

[132] Baek, S., Green, R. A., & Poole-Warren, L. A., *Journal of Biomedical Materials Research Part A***, 2014**, 102(8), 2743-2754.

[133] Kriparamanan, R.; Aswath, P.; Zhou, A.; Tang, L.; Nguyen, K. T., *J Nanosci Nanotechnol* **2006**, 6 (7), 1905-1919.

[134] Sonam, S.; Sathe, S. R.; Yim, E. K.; Sheetz, M. P.; Lim, C. T., *Sci Rep-Uk* **2016**, 6, 20415.

[135] John, G. R.; Lee, S. C.; Brosnan, C. F., *The Neuroscientist* **2003**, 9 (1), 10-22.

[136] Farina, C.; Aloisi, F.; Meinl, E., *Trends Immunol.* **2007**, 28 (3), 138-45.

[137] Streit, W. J.; Hurley, S. D.; McGraw, T. S.; Semple-Rowland, S. L., *J Neurosci Res* **2000**, 61 (1), 10-20.

[138] Brück, D.; Wenning, G. K.; Stefanova, N.; Fellner, L., *Neurobiol. Dis.* **2016**, 85, 262-274.

[139] Aloisi, F.; Borsellino, G.; Caré, A.; Testa, U.; Gallo, P.; Russo, G.; Peschle, C.; Levi, G., *Int. J. Dev. Neurosci.* **1995**, 13 (3), 265-274.

[140] Lins, C.; Borojevic, R., *Growth Factors* **2001**, 19 (3), 145-152.

[141] Torres-Platas, S. G.; Comeau, S.; Rachalski, A.; Dal Bo, G.; Cruceanu, C.; Turecki, G.; Giros, B.; Mechawar, N., *J Neuroinflammation* **2014**, 11 (1), 12.

[142] Schroder, K.; Hertzog, P. J.; Ravasi, T.; Hume, D. A., *J. Leukoc. Biol.* **2004**, 75 (2), 163-189.

[143] Miljkovic, D.; Momcilovic, M.; Stojanovic, I.; Stosic-Grujicic, S.; Ramic, Z.; Mostarica-Stojkovic, M., *J Neurosci Res* **2007**, 85 (16), 3598-606.

[144] Cavalcanti, Y. V. N.; Brelaz, M. C. A.; Neves, J. K. d. A. L.; Ferraz, J. C.; Pereira, V. R. A., *Pulmonary medicine* **2012**, 2012.

[145] Rubio, N.; Sanz-Rodriguez, F., *Virology* **2007**, 358 (1), 98-108.

[146] Roy, M.; Richard, J.-F.; Dumas, A.; Vallières, L., *J Neuroinflammation* **2012**, 9 (1), 18.

[147] Erta, M.; Quintana, A.; Hidalgo, *J., Int J Biol Sci* **2012**, 8 (9), 1254-1266.

[148] Hariri, R. J.; Chang, V. A.; Barie, P. S.; Wang, R. S.; Sharif, S. F.; Ghajar, J. B., *Brain Res* **1994**, 636 (1), 139-142.

[149] Ma, X.; Reynolds, S. L.; Baker, B. J.; Li, X.; Benveniste, E. N.; Qin, H., *The Journal of Immunology* **2010**, 184 (9), 4898-4906.

[150] Chiang, C.-S.; Stalder, A.; Samimi, A.; Campbell, I., *Dev. Neurosci.* **1994**, 16 (3-4), 212-221.

[151] Fattori, E.; Lazzaro, D.; Musiani, P.; Modesti, A.; Alonzi, T.; Ciliberto, G., Eur. *J. Neurosci.* **1995**, 7 (12), 2441-2449.

[152] Sawada, M.; Suzumura, A.; Itoh, Y.; Marunouchi, T., *Neurosci Lett* **1993**, 155 (2), 175-178.

[153] Awatsuji, H.; Furukawa, Y.; Hirota, M.; Murakami, Y.; Nii, S.; Furukawa, S.; Hayashi, K., *J Neurosci Res* **1993**, 34 (5), 539-545.

[154] Brodie, C., *FEBS Lett* **1996**, 394 (2), 117-120.

[155] Telias, M; Segal, M; Ben-Yosef, D. *F1000Research.* **2014**, 3:196. DOI 10.12688/f1000research.4943.2.

[156] Lovat, V.; Pantarotto, D.; Lagostena, L.; Cacciari, B.; Grandolfo, M.; Righi, M.; Spalluto, G.; Prato, M.; Ballerini, L., *Nano Lett* **2005**, 5 (6), 1107-1110.

[157] Mazzatenta, A.; Giugliano, M.; Campidelli, S.; Gambazzi, L.; Businaro, L.; Markram, H.; Prato, M.; Ballerini, L., *J Neurosci* **2007**, 27 (26), 6931-6936.

[158] Cellot, G.; Toma, F. M.; Varley, Z. K.; Laishram, J.; Villari, A.; Quintana, M.; Cipollone, S.; Prato, M.; Ballerini, L., *J Neurosci* **2011**, 31 (36), 12945-12953.

[159] Bosi, S.; Rauti, R.; Laishram, J.; Turco, A.; Lonardoni, D.; Nieus, T.; Prato, M.; Scaini, D.; Ballerini, L., *Scientific Reports (Nature Publisher Group)* **2015**, 5, 9562.

[160] Scarisbrick, I. A.; Radulovic, M.; Burda, J. E.; Larson, N.; Blaber, S. I.; Giannini, C.; Blaber, M.; Vandell, A. G., K., *Biological Chemistry* **2012,** 393 (5), 355-367.

[161] Padmanabhan, J.; Kyriakides, T. R., *Wiley Interdisciplinary Reviews: Nanomedicine and Nanobiotechnology* **2015**, 7 (3), 355-370.

[163] Gadegaard, N.; Mosler, S.; Larsen, N. B., *Macromol. Mater. Eng.* **2003**, 288 (1), 76-83.

[164] Baek, S.; Green, R. A.; Poole-Warren, L. A., *Acta Biomater* **2014**, 10 (7), 3048-3058.

[165] Wen, M.; Liu, H.; Zhang, F.; Zhu, Y.; Liu, D.; Tian, Y.; Wu, Q., *Chem. Commun*. **2009**, (30), 4530-4532.

[166] Bard, A. J.; Faulkner, L. R.; Leddy, J.; Zoski, C. G., *Electrochemical methods: fundamentals and applications*. Wiley New York: **1980**; Vol. 2.

[167] Stevens, N.; Rooney, M.; Bond, A.; Feldberg, S., *The Journal of Physical Chemistry A* **2001**, 105 (40), 9085-9093

[168] Kavanagh, E. T.; Loughlin, J. P.; Herbert, K. R.; Dockery, P.; Samall, A.; Doyle, K. M.; Gorman, A. M., *Biochem Biophys Res Commun* **2006**, 351 (4), 890-895.

[169] Rauti, R.; Lozano, N.; León, V.; Scaini, D.; Musto, M.; Rago, I.; Ulloa Severino, F. P.; Fabbro, A.; Casalis, L.; Vázquez, E., *Acs Nano* **2016**, 10 (4), 4459-4471.

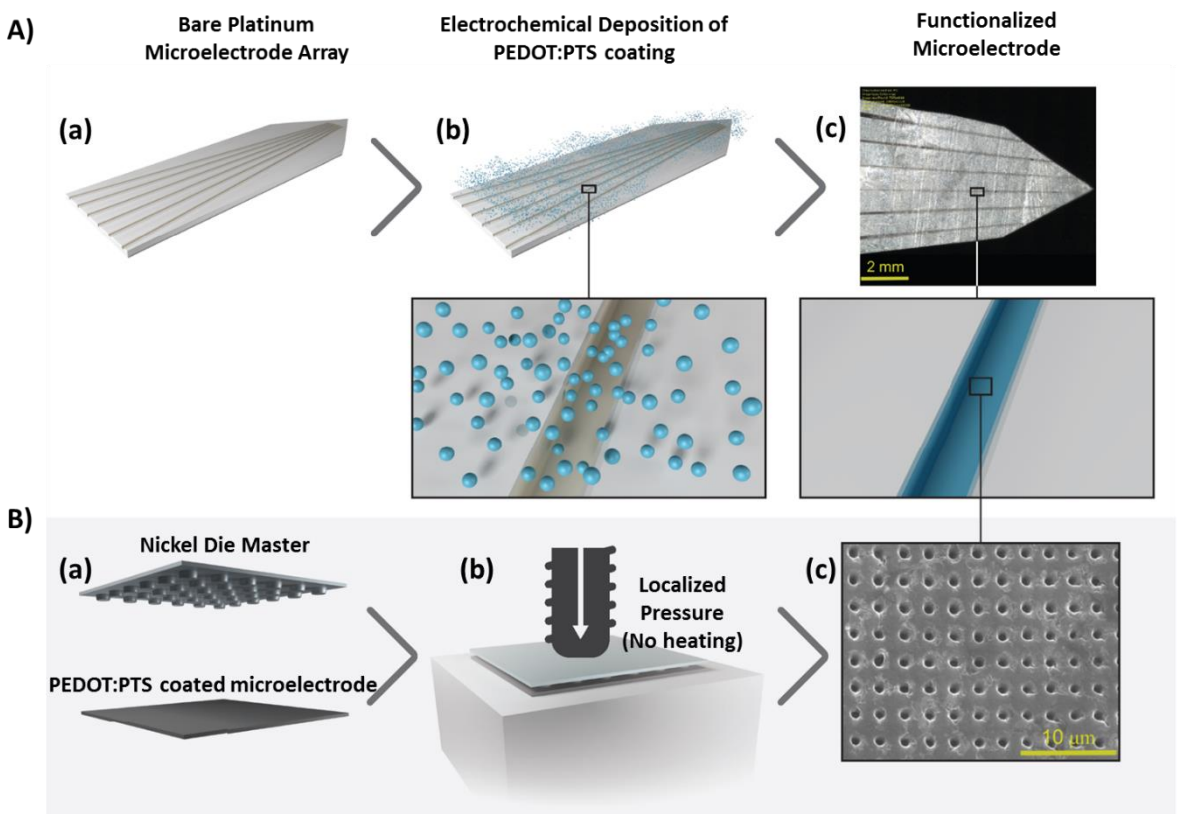

Figure 1. Microelectrode functionalization process. Upper panel A) describes the sequential steps taken on the bare platinum electrodes (a) electrodeposition of PEDOT:PTS coating (b), followed by the optical micrograph of the coated PEDOT:PTS microelectrode ready for the functionalization with the topography (c) Scale bar= 2mm, 10×. Bottom panel B) outlines the low temperature three-step die imprinting lithography process. This process starts with the micro-pit nickel die master and the PEDOT:PTS coated electrode (a). The nickel die was then pressed against the PEDOT:PTS coated microelectrode at a localized constant pressure of 1.9 metric tons per cm^2 for fifteen minutes at room temperature using parallel pressing plates. Finally, a scanning electron micrograph (SEM) of the micro-topographically functionalized PEDOT:PTS coated microelectrode is shown (c).

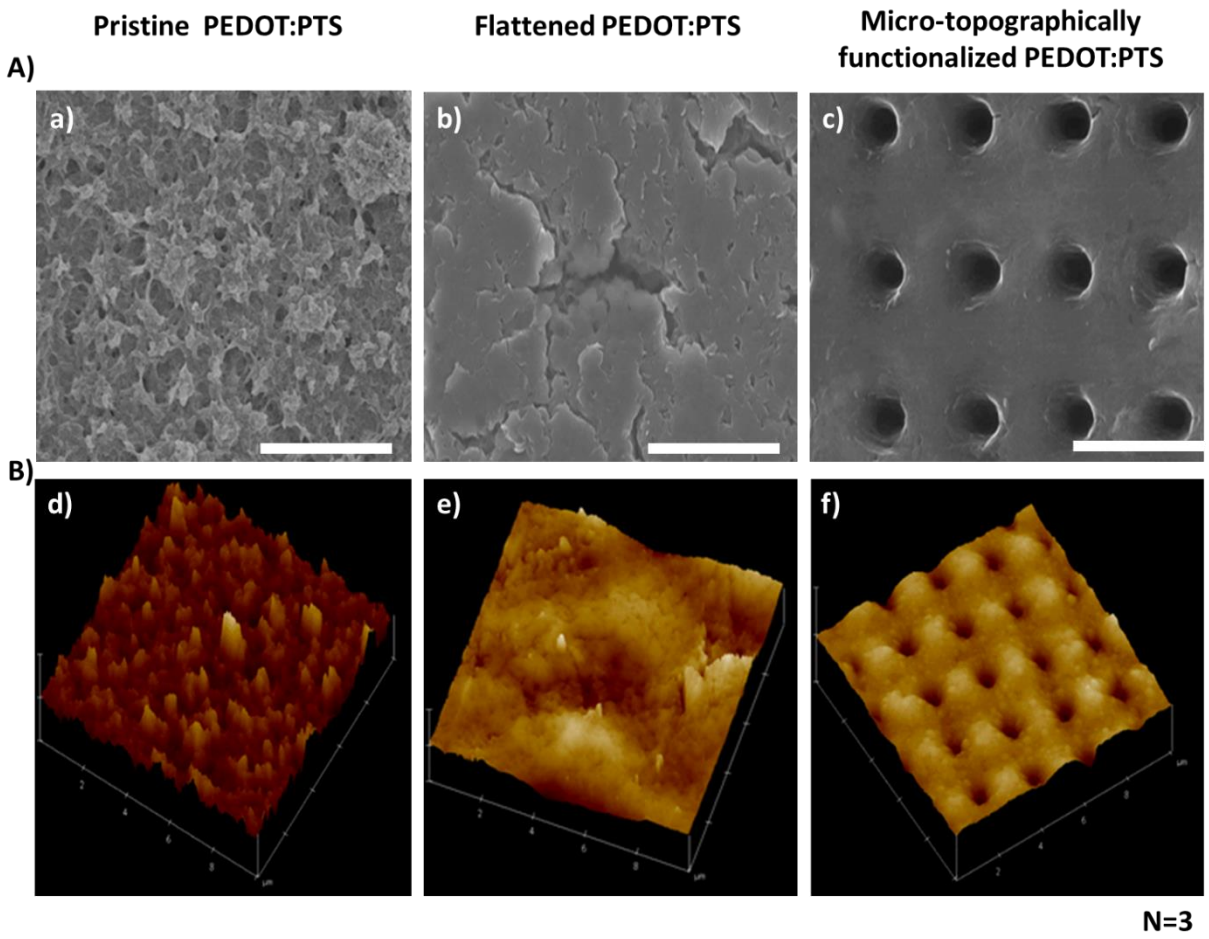

Figure 2. Microelectrode morphological physical characterization. Upper panel A). Scanning electron micrographs (SEM) (a-c) of pristine PEDOT:PTS, flattened PEDOT:PTS and the micro-topographically functionalized PEDOT:PTS coated microelectrodes. Scale bar = 3µm. B) Corresponding surface plots (d-f) of pristine PEDOT:PTS, flattened PEDOT:PTS and the micro-topographically functionalized microelectrodes on 10 μm^2 regions.

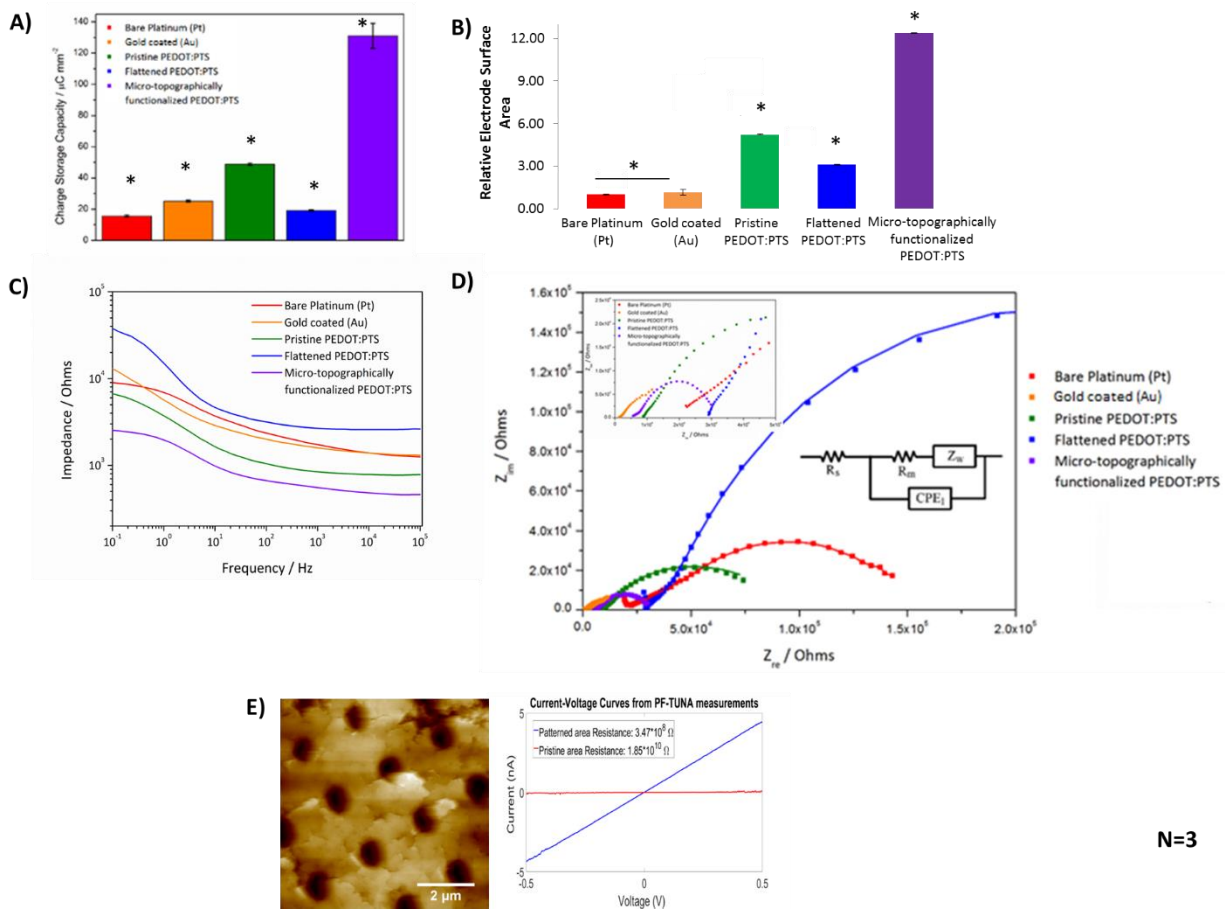

Figure 3. Electrochemical analysis of functionalized PEDOT:PTS coated microelectrodes. A) Cyclic voltammograms (CVs) bare platinum (Pt) and gold coated (Au) microelectrodes and pristine PEDOT:PTS, flattened PEDOT:PTS and micro-topographically functionalized PEDOT:PTS coated microelectrodes. CVs were recorded in 1X phosphate-buffered saline (PBS) at a scan rate of 100 mV s^{-1}. B) Relative electrode surface area calculated based on cyclic voltammograms (CVs) in 2.5 mol dm^{-3} $K_4[Fe(CN)_6]$ in 0.1 M KCl solution at a scan rate of 100 mV s^{-1}. The relative electrode surface area was estimated according to the Randles-Sevcik equation and the bare platinum (Pt) microelectrode was used as a reference. Bode (C) and Nyquist (D) plots comparing the EIS spectra of bare platinum (Pt) and gold coated (Au) microelectrodes and pristine PEDOT:PTS, flattened PEDOT:PTS and micro-topographically functionalized PEDOT:PTS coated microelectrodes. In addition, in D is shown the electrical equivalent circuit used to analyze experimental data and the low impedance regions. E) C-AFM micrograph of micro-topographically functionalized PEDOT:PTS coated microelectrode used for analysis and the corresponding I-V curves recorded at selective positions, non-patterned region and patterned region (pit) on the micro-topographically functionalized microelectrode. C-AFM tips (coated with Platinum/Iridium) were used as the mobile counter electrode to contact the SWCNTs (PeakForce-TUNA tips, Bruker). For a schematic of the set-up, see **Figure S4**. The voltage bias was ramped between -500mV and 500mV. The data was then analyzed by NanoScope Analysis (version 1.5, Bruker) and Matlab (version 2016 a).Results are ± STD, ★ = $p < 0.05$. N=3

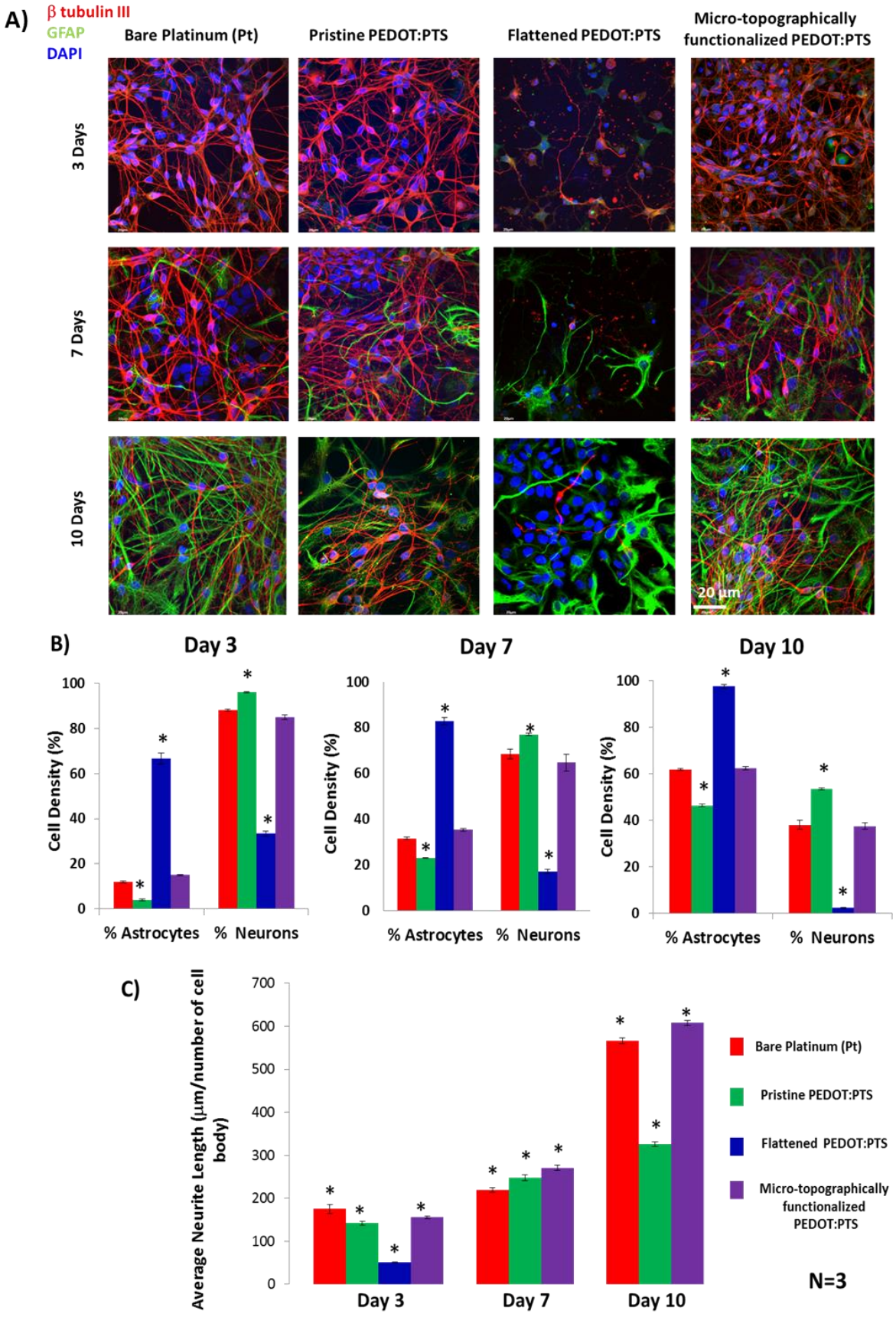

Figure 4. Cellular and morphometric analysis of functionalized electrodes. A) Fluorescent images of primary ventral mesencephalic (VM) mixed cell population grown on each of the bare platinum (Pt) and functionalized PEDOT:PTS coated electrodes for three, seven and ten

days in culture. Neurons are visualized by anti β-tubulin III, in red, astrocyte cells by anti-GFAP, in green and nuclei are visualized by DAPI, in blue. Bar = 20 μm, objective 60× magnification. Cell density (%) analysis of astrocytes and neurons presence on each of the electrodes is presented in B). An overall significant ($p < 0.05$) decrease in viability of neurons and astrocytes density was observed in flattened PEDOT:PTS coated electrodes. Neural length analysis of electrodes presented in C) showed with significant ($p < 0.05$) longer neurite lengths the neurons grown on micro-topographically functionalized PEDOT:PTS coated electrodes. ★ = $p< 0.05$.

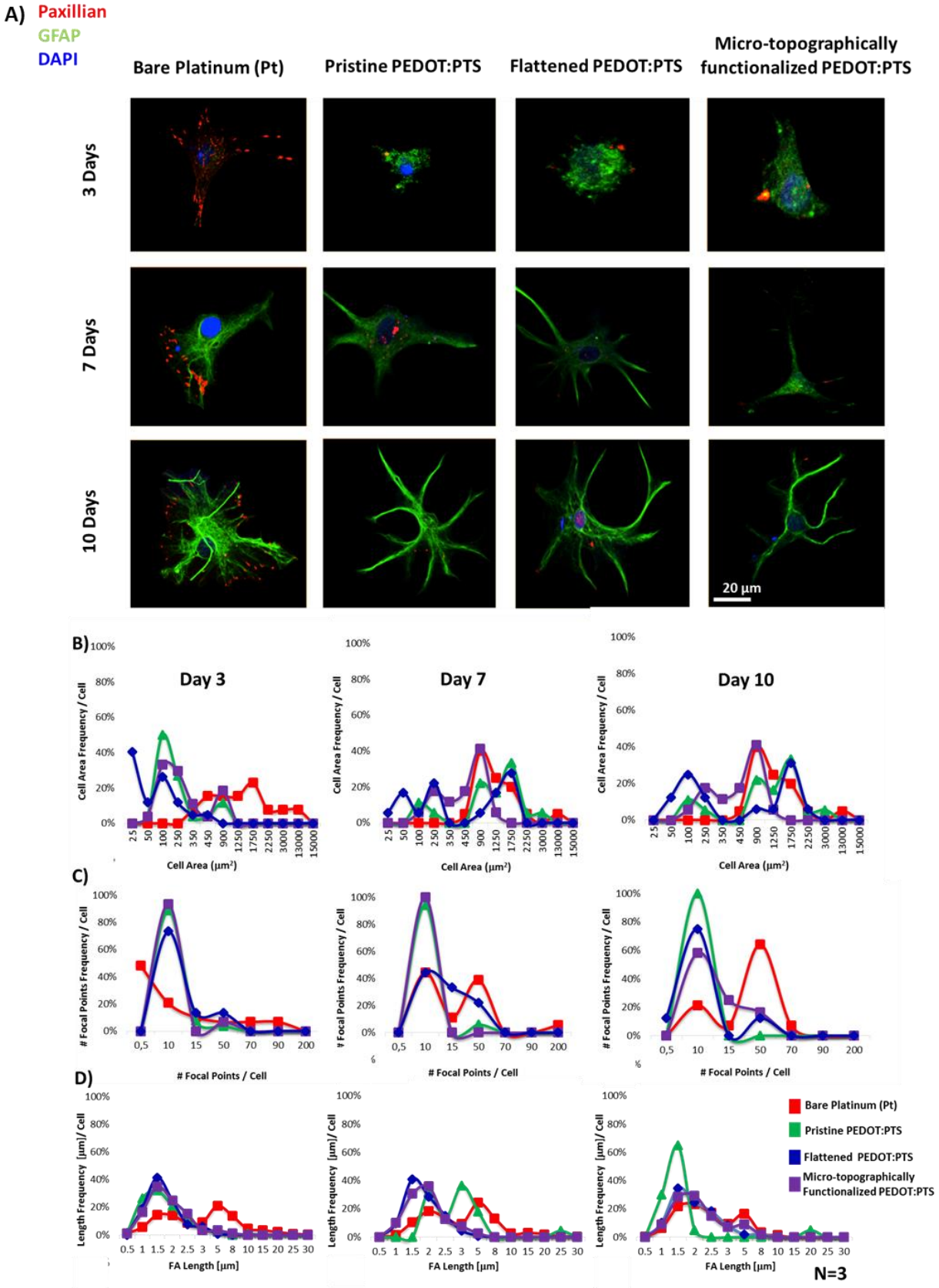

Figure 5. Morpho-adhesion characteristics of astrocyte presence in the functionalized electrodes towards astrocyte reactivity indication. A) Selective fluorescent images of astrocytes from primary ventral mesencephalic (VM) mixed cell population grown on each of the bare platinum (Pt) and functionalized PEDOT:PTS coated electrodes for three, seven and ten days in culture. Astrocytes are visualized by anti-GFAP, in green, formation of focal adhesion

contacts by anti-Paxillian, in red and nuclei are visualized by DAPI, in blue. Bar = 20 µm, objective 60× magnification. Frequency distribution in time (three, seven, and ten days) of cytoplasm astrocyte areas (µm^2) on bare platinum (Pt) and functionalized PEDOT:PTS coated electrodes is presented in B). The frequency distribution of astrocyte areas on micro-topographically functionalized PEDOT:PTS coated electrodes showed the lowest frequencies over time. C) represents the frequency distribution of the astrocyte focal adhesion contact numbers per cell and their corresponding length frequency distribution over time in D).

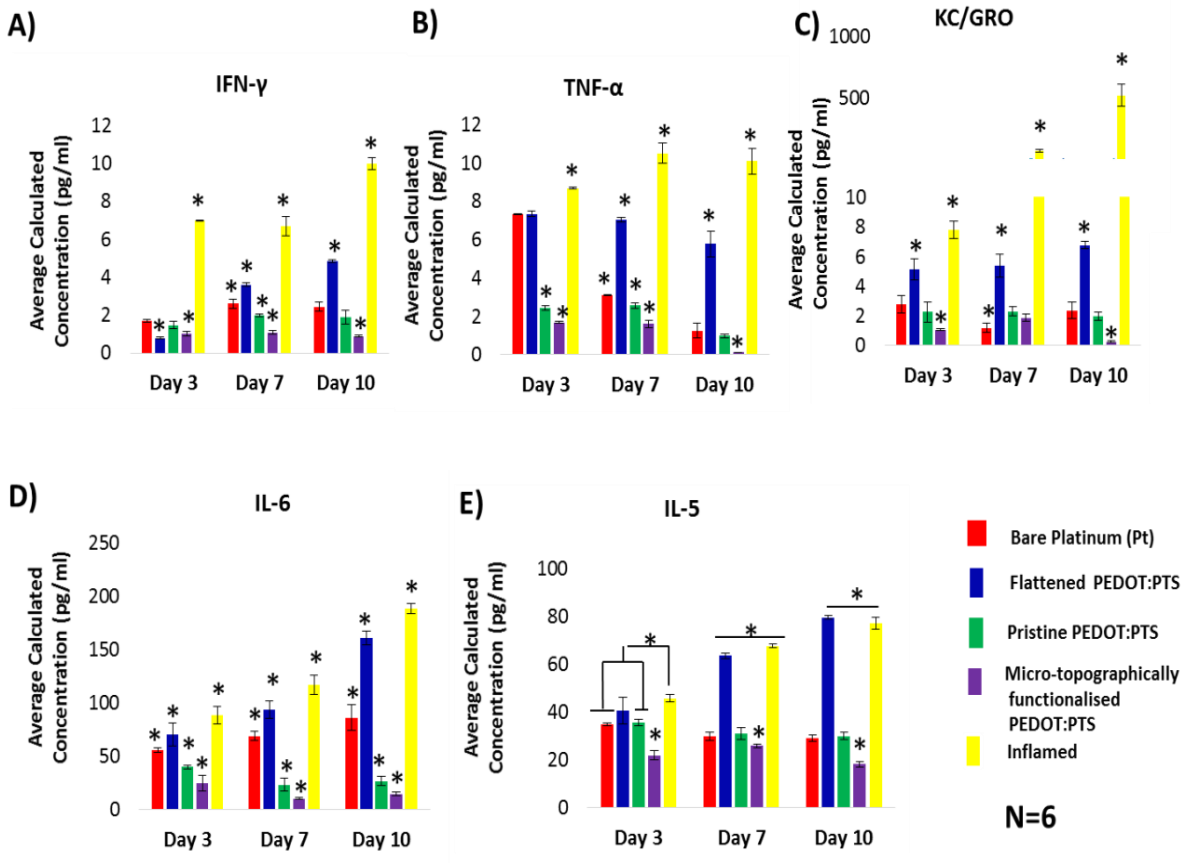

Figure 6. Comparative gliosis derived cytokines and chemokine factor profiling for interferon-γ (IFN-γ;A), tumor necrosis factor- α (TNF-α;B), chemokine factor CXCL-1 (KC/GRO;C), interleukin-6 (IL-6;D) and interleukin-5 (IL-5;E). The release expression of each of the signaling molecules is analyzed from primary ventral mesencephalic (VM) mixed cell population supernatants collected at day three, seven and ten days on bare platinum (Pt) and functionalized PEDOT:PTS coated electrodes. An important effect is seen on the micro-topographically functionalized PEDOT:PTS coated electrodes, which presented significantly and consistently low release profiles for each cytokine and chemokine factor analyzed. Results are ± STD, ★ = $p < 0.05$.

Table 1. Microelectrode physical properties. Values of experimental mean surface roughness (Ra) and mean surface area (SA) measurements over 10 μm^2 regions. The data represent the mean of 15 measurements from three different replicas. Results are ± SD, N=3.

Microelectrodes	Average Roughness R_a [nm]	Average Surface Area [nm^2]
Bare platinum (Pt)	1.96 ± 0.22	1.05 E+10 ± 35.35 E+06
Pristine PEDOT:PTS	85.16 ± 16.94	1.74 E+10 ± 93.34 E+06
Flattened PEDOT:PTS	52.59 ± 6.16	1.32 E+10 ± 71.42 E+06
Micro-topographically functionalized PEDOT:PTS	76.10 ± 17.21	2.35 E+10 ± 51.77 E+06

Table 2. Electrochemical performance and stability of functionalized PEDOT:PTS coated microelectrodes. The initial and the final charge storage capacity (CSC) was evaluated from the cathodic region of cyclic voltammograms (CVs) recorded in 1X phosphate-buffered saline (PBS) at 100 mV s^{-1} scan rate (Potential range: -1 V to 0.4 V vs. Ag/AgCl). The corresponding loss was calculated after 500 cycles. Results are ±SD, N=3.

	Bare Platinum (Pt)	Gold Coated (Au)	Pristine PEDOT:PTS	Flattened PEDOT:PTS	Micro- topographically functionalized PEDOT:PTS
Initial CSC [$\mu C\ mm^{-2}$]	15.57 ± 0.66	25.12 ± 0.66	48.82 ± 0.49	19.09 ± 0.77	131.01 ± 8.05
Final CSC [$\mu C\ mm^{-2}$]	4.36 ± 0.17	15.79 ± 0.31	31.01 ± 0.11	0.38 ± 0.04	96.41 ± 22.23
Electroactivity loss [%]	72.10± 1.61	37.17 ± 0.23	36.50 ± 0.41	98.1 ± 1.52	26.42 ± 6.33

Table 3. Summary of the calculated resistance values (R_m), solution resistance values (R_s), constant phase element parameters (P – pseudocapacitance, n – exponent) and Warburg coefficients (W_{sr}, W_{sc}) of bare platinum (Pt) and gold coated (Au) microelectrodes and pristine PEDOT:PTS, flattened PEDOT:PTS and micro-topographically functionalized PEDOT:PTS coated microelectrodes after equivalent circuit analysis. Results are ± STD. N=3

		Bare Platinum (Pt)	Gold Coated (Au)	Pristine PEDOT:PTS	Flattened PEDOT:PTS	Micro-topographically functionalized PEDOT:PTS
R_m, [kOhms]		40.28 ± 0.63	23.61 ± 1.28	12.01 ± 1.53	357.77 ± 14.64	3.11 ± 0.13
R_s, [kOhms]		3.00 ± 0.16	0.92 ± 0.02	8.59 ± 0.11	27.50 ± 0.32	4.41 ± 0.04
CPE_1	P_2	4.57E-6 ± 0.06E-6	3.88E-4 ± 0.09E-4	6.40E-6 ± 0.40E-6	9.89E-6 ± 0.36E-6	1.03E-5 ± 0.05E-5
	n_2	0.143 ± 0.002	0.151 ± 0.003	0.538 ± 0.013	0.381 ± 0.007	0.323 ± 0.010
Z_w:	W_{sr1}	4.50E5 ± 0.21E5	-	1.45E5 ± 0.05E5	-	5.01E4 ± 0.12E4
	W_{sc1}	0.525 ± 0.099		0.377 ± 0.015		0.422 ± 0.014
CPE_2:	P_1	-	7.39E-5 ± 0.19E-5	-	1.05E-6 ± 0.03E-6	-
	n_1		0.629 ± 0.009		1 ± 0.015	

Micro-topographically functionalized neuroelectrode interfaces composed of micro-pits are fabricated by a temperature low-imprinting lithography enhancing electrical conductivity and stability. Further, the micro-pit functionalized microelectrodes promote reduction of reactive astrocytes presence while supporting neural outgrowth and neural network functionality.

Keywords neural interfaces, functionalization, electrodes, astrogliosis, inflammation

Catalina Vallejo-Giraldo, Katarzyna Krukiewicz, Ivo Calaresu, Jingyuan Zhu, Matteo Palma, Marc Fernandez, Benjamin G, Nathalia Peixoto, Nazar Farid, Gerard O'Connor, Laura Ballerini, Abhay Pandit, and Manus Jonathan Paul Biggs*

Attenuated Glial Reactivity on Topographically Functionalized Poly(3,4-Ethylenedioxythiophene):P-Toluene Sulfonate (PEDOT:PTS) Neuroelectrodes Fabricated by Microimprint Lithography

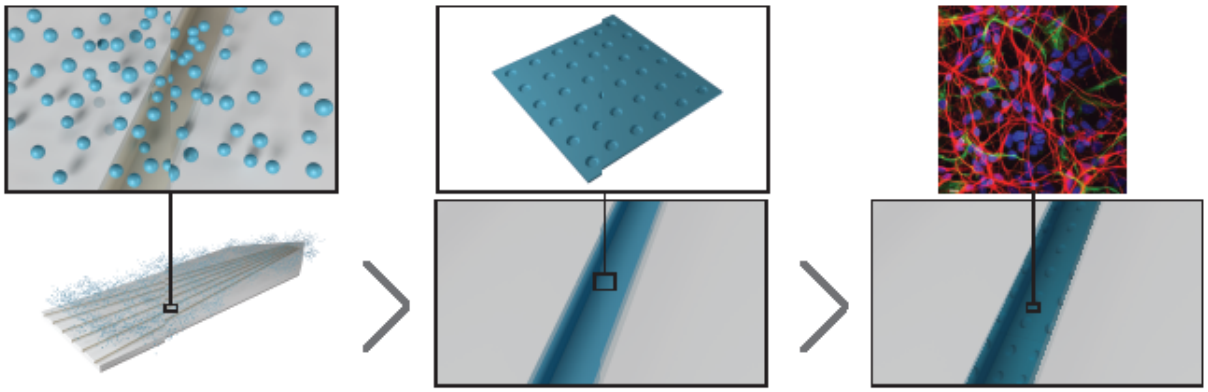

Supporting Information

Attenuated Glial Reactivity on Topographically Functionalized Poly(3,4-Ethylenedioxythiophene):P-Toluene Sulfonate (PEDOT:PTS) Neuroelectrodes Fabricated by Microimprint Lithography

Catalina Vallejo-Giraldo, Katarzyna Krukiewicz, Ivo Calaresu, Jingyuan Zhu, Matteo Palma, Marc Fernandez, Benjamin G, Nathalia Peixoto, Nazar Farid, Gerard O'Connor, Laura Ballerini, Abhay Pandit, and Manus Jonathan Paul Biggs*

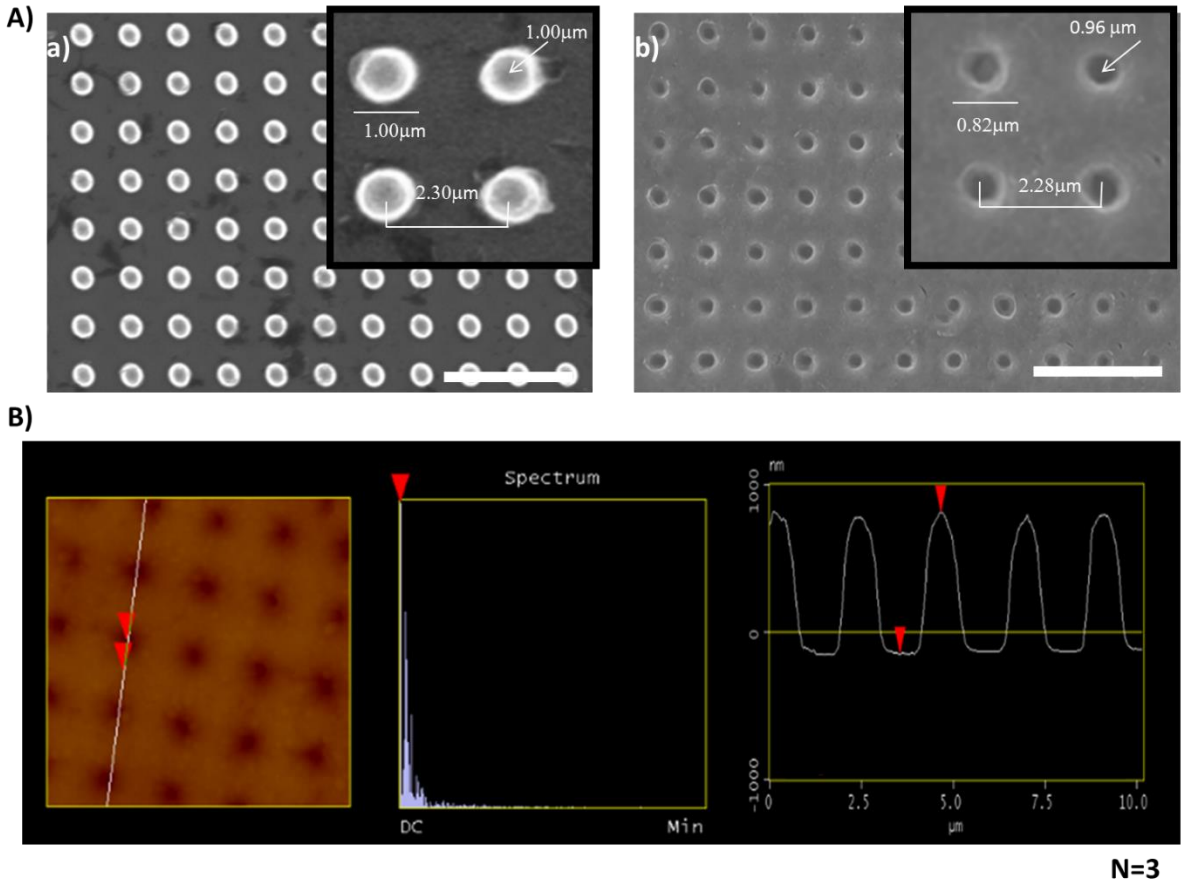

Figure S1. Micro-topographically functionalized microelectrodes. Upper panel A) Scanning electron micrographs (SEM) of the nickel die master utilized for the low temperature three-step die imprinting lithography process (a) the micro-topographically functionalized substrate with ordered array of micro-pits produced on PEDOT:PTS coated microelectrodes by low temperature three-step die imprinting lithography process (b). Scale bar = 10 µm. In the insets, the pit, interpit and depth dimensions are detailed. B) Atomic-force microscopy (AFM) sectional analysis of the micro-topographically functionalized PEDOT:PTS coated microelectrode over a region of 10 μm^2 area reflecting the vertical distance of the pit patterned

transferred of 0.96 ± 0.07 µm. Fifteen measurements were taken from three different replicas. Results are ± STD.

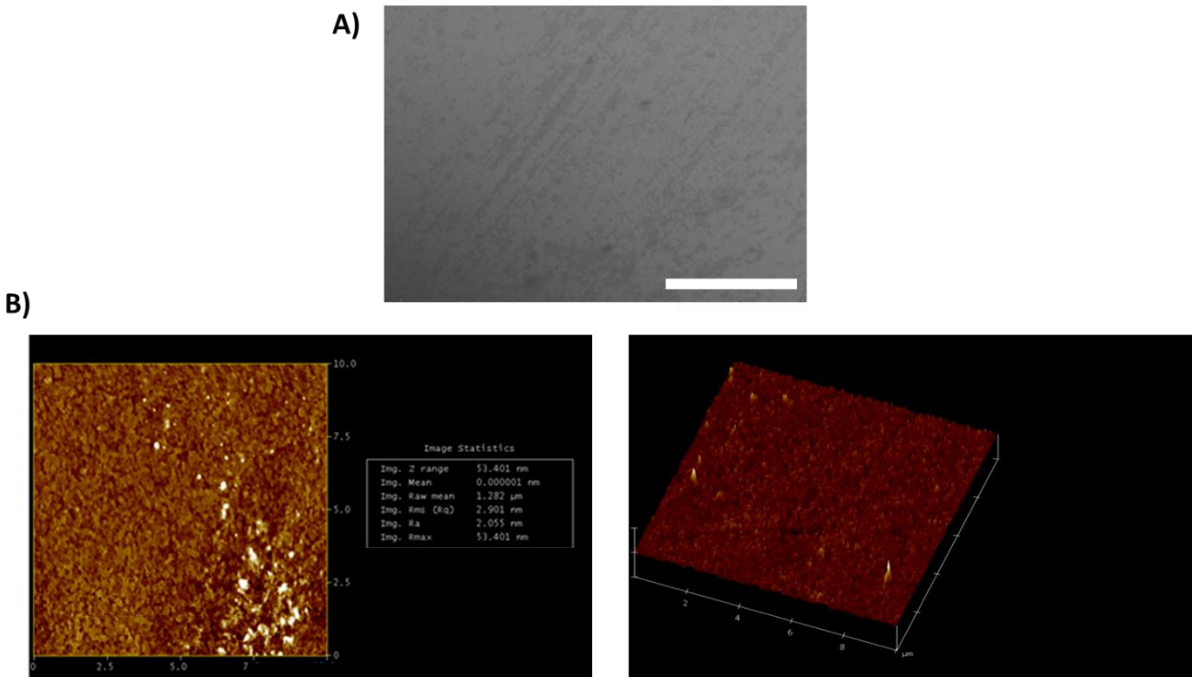

Figure S2. Bare platinum (Pt) morphological characterization A). Scanning electron micrograph (SEM) of bare platinum (Pt) microelectrodes, and corresponding mean surface roughness (R_a) (B). Scale bar = 3µm

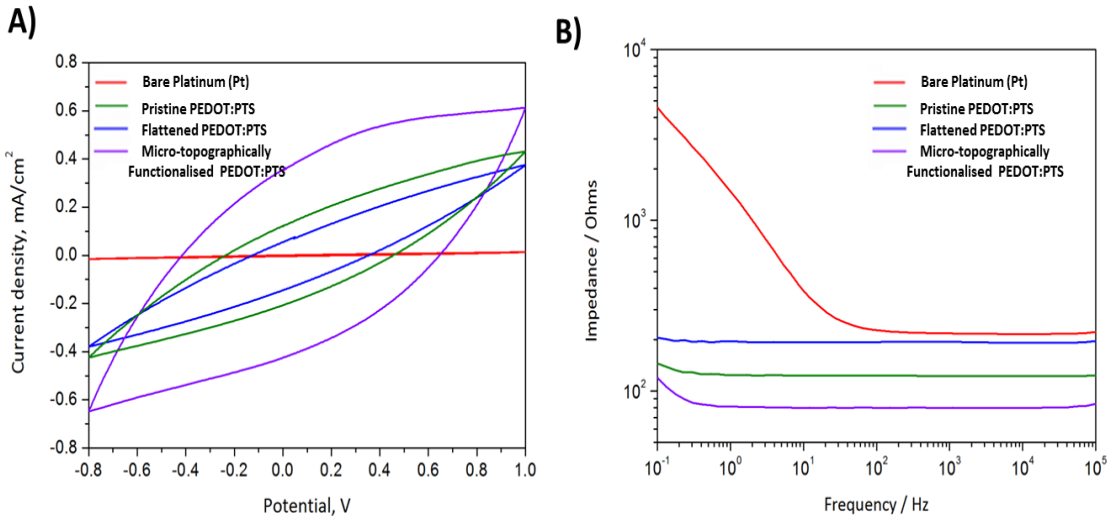

C)

	Bare Platinum (Pt)	Pristine PEDOT:PTS	Flattened PEDOT:PTS	Micro-topographically functionalised PEDOT:PTS
CSC [mC cm^{-2}]	2.38 ± 0.04	66.48 ± 0.49	54.90 ± 0.63	122.04 ± 0.27

N=3

Figure S3. Electrochemical analysis of functionalized PEDOT:PTS coated macro electrode (1.6 cm^2). A) Cyclic voltammograms (CVs) bare platinum (Pt) and pristine PEDOT:PTS, flattened PEDOT:PTS and micro-topographically functionalized PEDOT:PTS coated electrodes. CVs were recorded in 1X phosphate-buffered saline (PBS) at a scan rate of 100 mV s^{-1}. B) Bode plots comparing the EIS spectra of bare platinum (Pt) and pristine PEDOT:PTS, flattened PEDOT:PTS and micro-topographically functionalized PEDOT:PTS coated electrodes. C) Table summarizing the charge storage capacity (CSC) of large bare platinum (Pt) and pristine PEDOT:PTS, flattened PEDOT:PTS and micro-topographically functionalized PEDOT:PTS coated electrodes. CSC was evaluated from the cathodic region of cyclic voltammograms (CVs) recorded in 1X phosphate-buffered saline (PBS) at 100 mV s^{-1} scan rate (Potential range: -1 V to 0.4 V vs. Ag/AgCl). Results are ± STD, ★ = $p< 0.05$.

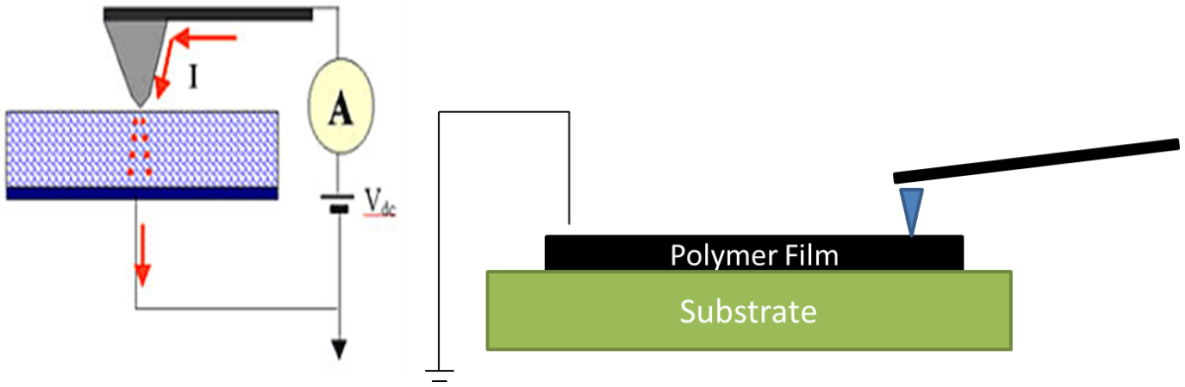

Figure S4. Schematic of Conductive AFM (PF-TUNA) used for the evaluation of the micro-functionalized microelectrodes conductive profile. By using the moving probe as mobile electrode, the current was flowing through the metal-coated tip and the conducting sample which was grounded.

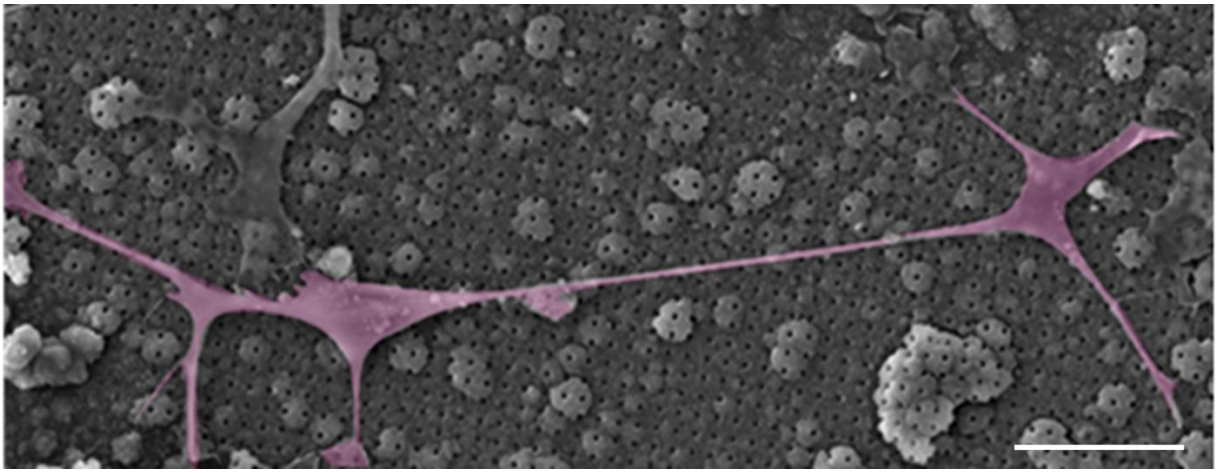

Figure S5. Ventral mesencephalic cells (VM) adhered on micro-topographically functionalized electrodes. Scanning electron micrograph (SEM) of primary VM mixed cell population adhered on micro-topographically functionalized PEDOT:PTS coated electrodes. Scale bar= 50 µm.

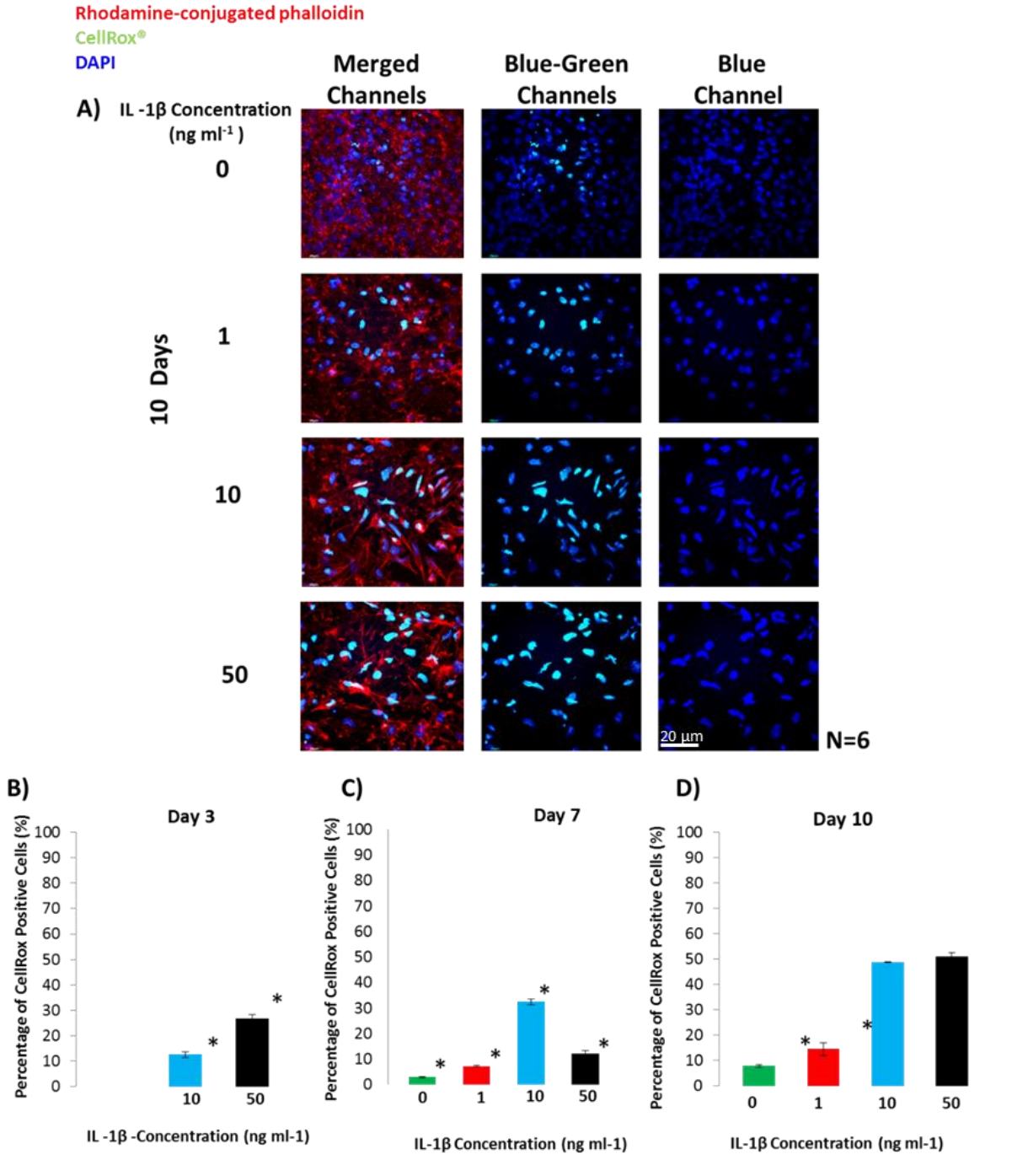

Figure S6. CellROX® expression on primary ventral mesencephalic (VM) mixed cell population grown on sterile Thermanox® Plastic Coverslips with 13 mm diameter (NUNCTM brand products). Cultures were stimulated with interleukin- 1β (IL-1β) at 1, 10 and 50 ng ml^{-1} and control. A) Fluorescent images of VM mixed cell population grown on sterile Thermanox® Plastic Coverslip over a period of three, seven and ten days showing CellROX® expression in green, actin in red rhodamine-conjugated phalloidin and nuclei in blue, DAPI. Bar = 20 µm, objective 60× magnification. (B-D) show the percentage of CellROX® nuclei colocalization quantified after stimulus with interleukin-1β (IL-1β) at 1, 10 and 50 ng ml^{-1} and control. Elevated levels of CellROX® on VM mixed cell population were seen after a stimulus of 10 ng ml^{-1} of IL-1 β and 50 ng ml^{-1} over ten days in culture, resulting in an increase of oxidative stress species presence as a response of inflammation. ★ = $p < 0.05$.

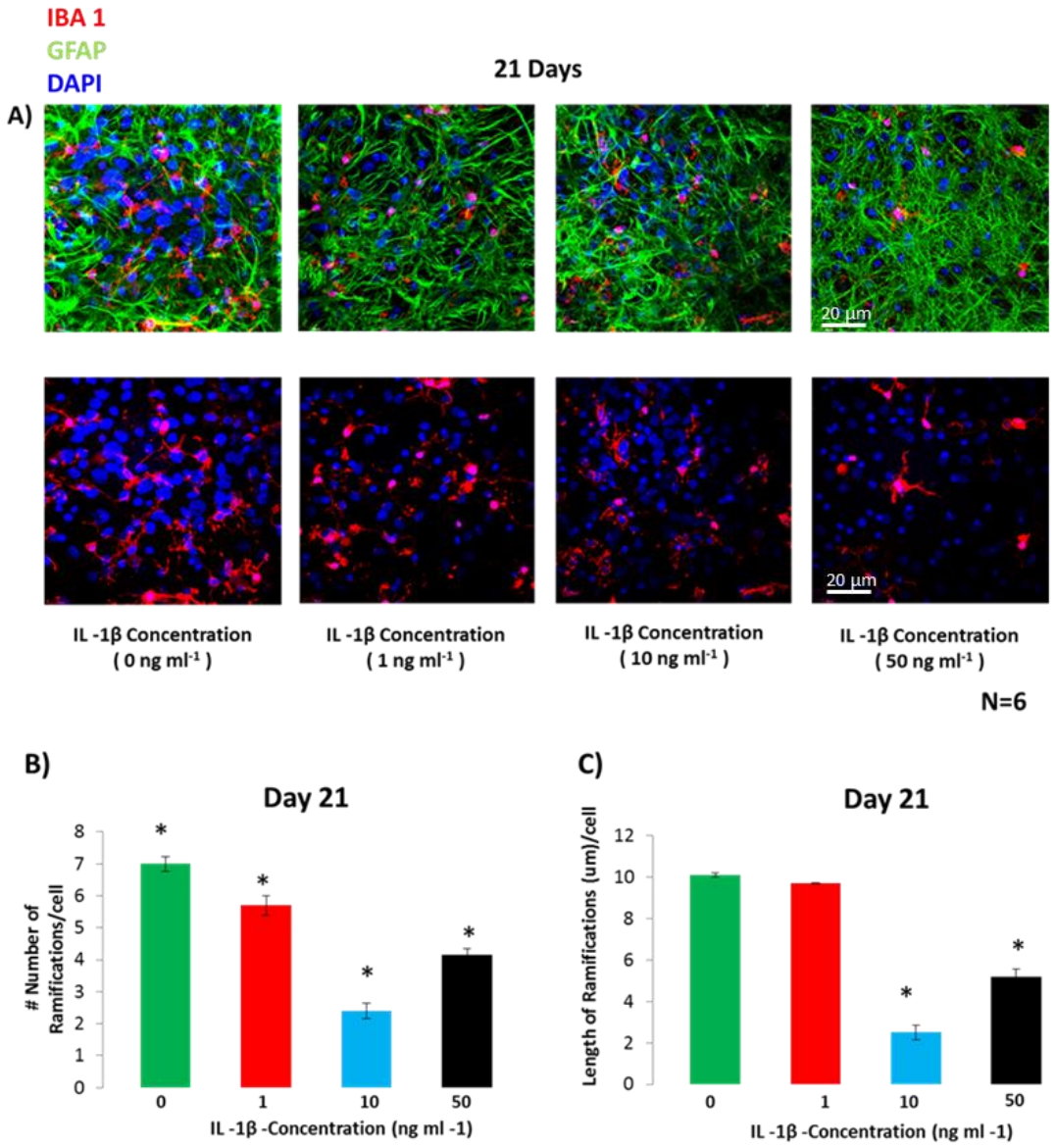

Figure S7. Morphological characterization of activated microglia population from primary ventral mesencephalic (VM) mixed cells under stimulus of interleukin- 1β (IL-1β) at 1, 10 and 50 ng ml^{-1} and control concentrations after 21 days in culture. A) Fluorescent images of astrocytes and microglia from VM mixed cell population grown on sterile Thermanox® Plastic Coverslips with 13 mm diameter (NUNCTM) brand products over a period of 21 days. Astrocytes are visualized by anti-GFAP, in green and microglia are visualized by Iba-1, in red, and nuclei are visualized by DAPI, in blue. Bar = 20 µm, objective 60× magnification. The number of microglia ramifications B) and their length C) were quantified following methods detailed in [141] as indicators of activated microglia. Significant differences ($p<0.05$) were observed in the number and length of microglia ramifications cultured under stimulus of 10 ng ml^{-1} IL-1β compared to controls and to the other IL-1β concentrations used. Overall, microglia morphologies under stimulus of 10 ng ml^{-1} IL-1β resemble microglia amoeboid morphologies. ★ = $p< 0.05$.

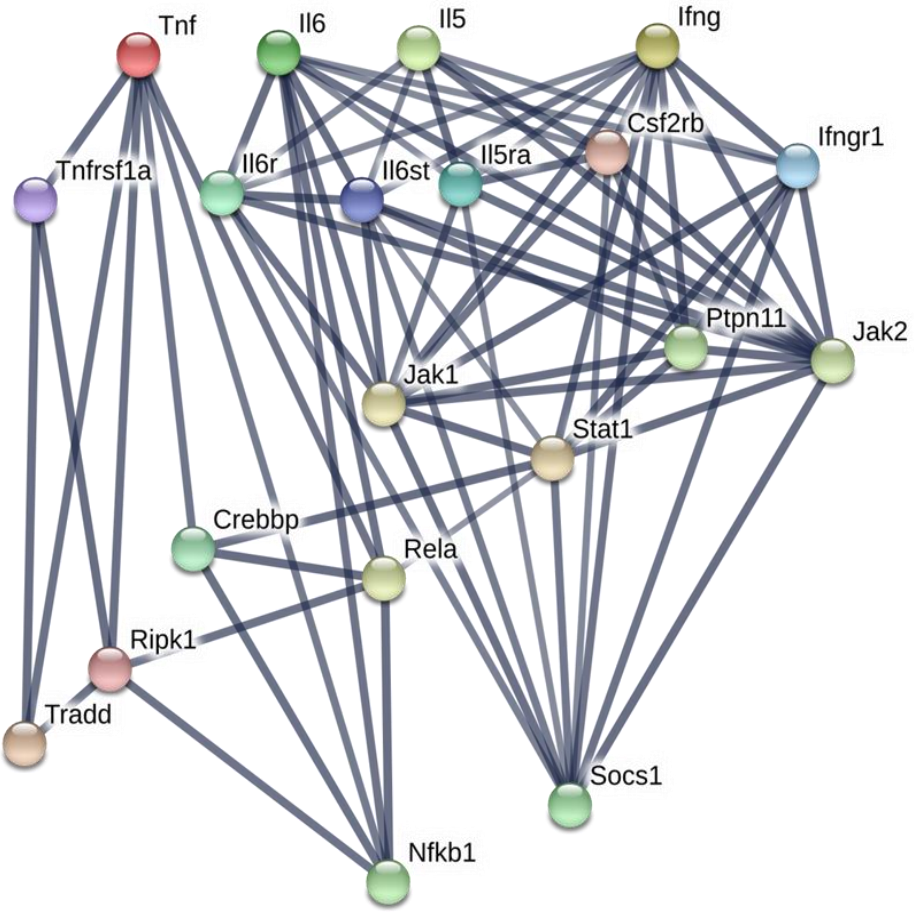

Figure S8. Molecular network induced by cytokines TNFα, IL-6, IL-5 and IFN-γ secreted by primary ventral mesencephalic (VM) mixed cells. Each node represents a single protein molecule encoded by genes. Colored nodes indicate query proteins and first shell of interactors. The lines between the nodes indicate high confidence (>0.7) predicted interactions based on experimentally determined databases, co-expression, and co-occurance.

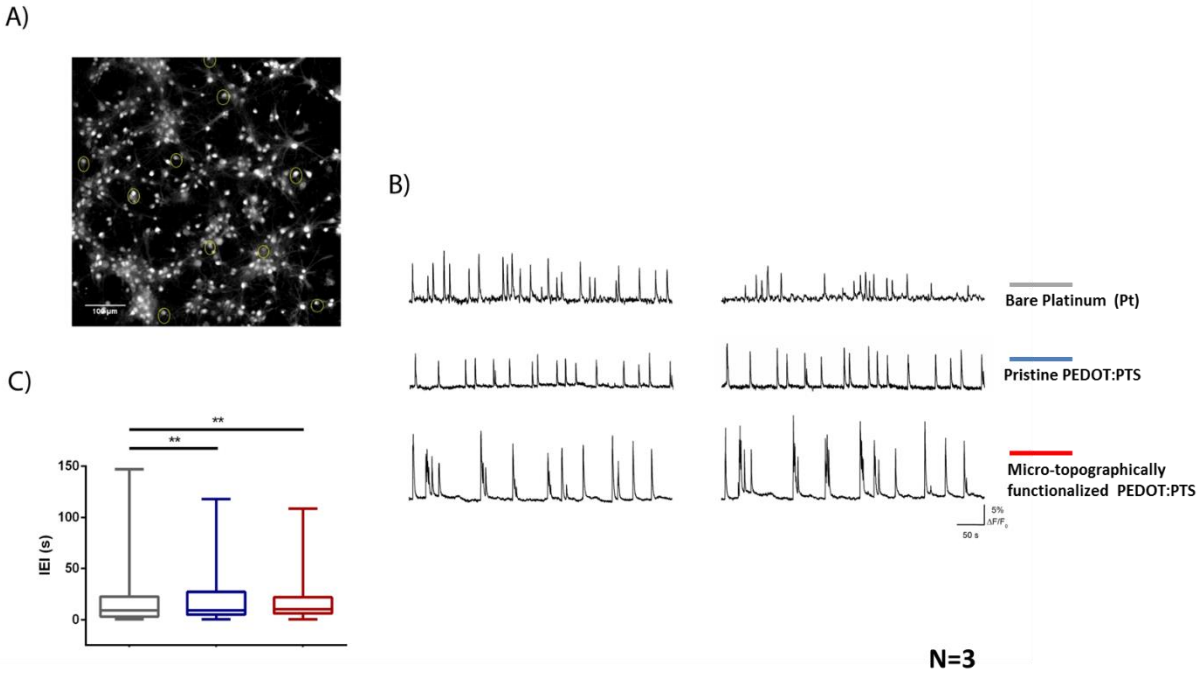

Figure S9. Spontaneous network activity on bare platinum electrodes, pristine PEDOT:PTS and micro-topographically functionalized PEDOT:PTS coated electrodes. A) Snapshots of a representative field of hippocampal dissociated cultures labeled with Oregon green 488-BAPTA-1 AM. Yellow circles indicate the selected regions of interest (ROI) from which calcium events were measured. B) Two representative traces for each condition show the neuronal spontaneous activity, calcium transients are expressed as fractional amplitude increase ($\Delta F/F_0$). C) Box plots summarize the distribution of the inter-event intervals (IEIs). **$p < 0.01$ Kruskal-Wallis test on ranks suggested a difference in the IEIs distribution among the different substrates, regardless the IEIs mean or median values, data are reported as mean ± SD.

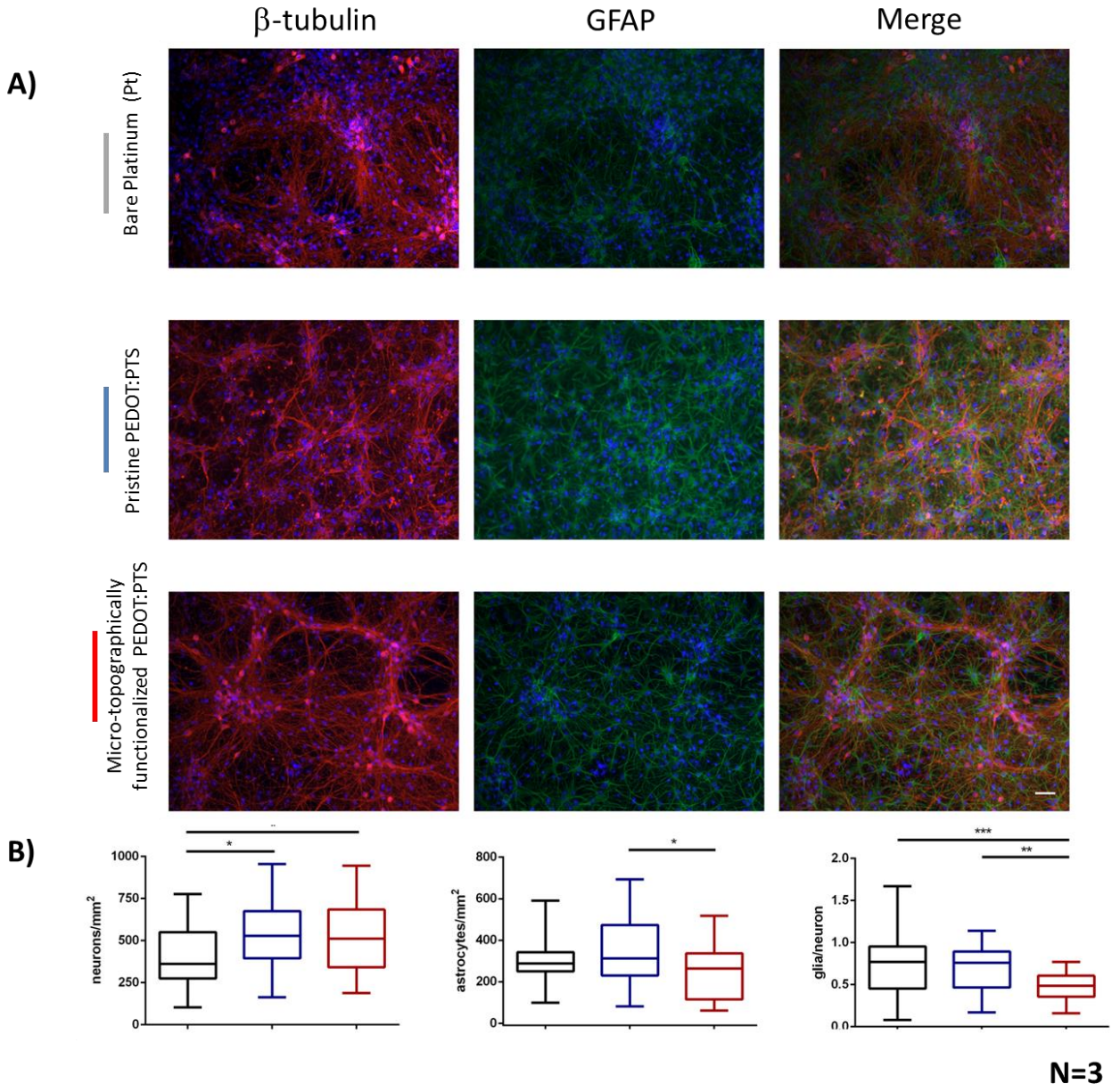

Figure S10. Synaptic network formation supported by bare platinum electrodes, pristine PEDOT:PTS and micro-topographically functionalized PEDOT:PTS coated electrodes. A) Epifluorescence micrographs of immunolabeled cultures, large fields are shown at 10× magnifications. Neurons are visualized by anti β-tubulin III, in red, glial cells by anti-GFAP, in green, and nuclei by DAPI, in blue. Scale bar = 100 µm. B) Plots summarize neuronal (left) and astrocytes (middle) densities in the three conditions. Astrocyte-to-neuron ratios (right) are also

shown for all samples. *p < 0.05, **p < 0.01 and ***p < 0.001, one-way ANOVA p-value was adjusted for multiple comparison with Tukey's correction, data are mean ± SD.

Table S1. X-ray photoelectron spectroscopy (XPS) analysis of the elemental composition of the micro-topographically functionalized PEDOT:PTS coated microelectrodes looking at the nickel residual presence from nickel die master used in the low temperature three-step die imprinting lithography process. Ni 2p atomic percentage was at the noise level. N=3.

	Atomic Composition [%]							
	C 1s	O 1s	Ni 2p	S 2p	N 1s	Na 1s	P 2p	Cl 2p
Micro-topographically functionalized PEDOT:PTS coated microelectrode	70.52	16.63	0.18	1.76	10.32	0.18	0.42	0.00